



In situ trace element compositions and U—Pb ages of cassiterite from tin-polymetallic deposits in the Dachang district, Guangxi, China: Implications for ore genesis and exploration

Jiali Cai ^{a,b}, Wenchao Su ^{a,*}, Nengping Shen ^a, Junyi Pan ^{c,*}, Hai Zhao ^d

^a State Key Laboratory of Ore Deposit Geochemistry, Institute of Geochemistry, Chinese Academy of Sciences, Guiyang 550081, China

^b University of Chinese Academy of Sciences, Beijing 100039, China

^c State Key Laboratory for Mineral Deposits Research, Institute of Geo-Fluids, Frontiers Science Center for Critical Earth Material Cycling, School of Earth Sciences and Engineering, Nanjing University, Nanjing 210046, China

^d Department of Tourism and Geography, Tongren University 554300, China



ARTICLE INFO

Keywords:

Cassiterite U—Pb dating

Trace elements

Tongkeng and Huile tin-polymetallic deposits

Dachang district

ABSTRACT

The Dachang tin-polymetallic district in southwest China is one of the largest tin ore fields in the world containing approximately 1.5 Mt. Sn, 6.8 Mt. Zn, 1.8 Mt. Pb, 1.4 Mt. Sb, 0.4 Mt. Cu and other critical metals. Both cassiterite-sulfide and Zn—Cu skarn mineralization occur as stratiforms, veins, and stockworks and are hosted in the Mid-Upper Devonian carbonate-rich sediments adjacent to the underlying Late Cretaceous Longxianggai granite pluton and/or the granite/diorite porphyry dikes. The Tongkeng and Huile deposits are typical stratiform- and vein-type tin-polymetallic deposits in the district. Previous studies suggest a genetic link between these tin-polymetallic deposits and the prolonged Longxianggai granite which was dated to have emplaced for multiple stages within ca. 91–97 Ma. However, existing constraints on the timing of tin mineralization display a broad range at 90–96 Ma, whereas the accuracy and precision of these ages are less satisfactory. These ages are broadly overlapping with both the prolonged Longxianggai granite and the porphyry dikes (91 Ma), thus gives rise to question on their genetic association, which is a question of importance for ore exploration in the district.

In this study, a large number of measurements of laser ablation-inductively coupled plasma-mass spectrometry (LA-ICP-MS) trace elements and U—Pb dating on cassiterites from the Tongkeng and Huile deposits was performed and their mineralization ages with hitherto the best accuracy and precision were obtained. LA-ICP-MS trace element analyses show that cassiterites from the Tongkeng and Huile deposits contain concentrations of Fe, W, Nb, and Ta characteristic of granitic-related skarn-type tin mineralization. U—Pb dating on cassiterites from 391 spots analyses yielded well-constrained ages of 91.13 ± 0.61 Ma to 89.46 ± 0.47 Ma for the Tongkeng deposit and 89.0 ± 1.3 Ma for the Huile deposit. These ages are apparently younger than the dominated equigranular phase of the Longxianggai pluton, but they agree well with the emplacement ages of the porphyritic granite represented either by the latest phase of the Longxianggai granite or the granite porphyry dikes (ca. 91 Ma). This suggests that the tin-polymetallic deposits in the Dachang district were most likely genetically associated with later, higher evolved granitic phases in the district. In this regard, the dike-hosting fault systems were most likely served as fluid conduits and their surrounding host rocks are favorable targets for ore exploration in the Dachang district.

1. Introduction

The Dachang tin-polymetallic district, Guangxi Autonomous Region, China, is one of the largest tin ore fields in the world containing approximately 1.5 Mt. Sn, 6.8 Mt. Zn, 1.8 Mt. Pb, 1.4 Mt. Sb, 0.4 Mt. Cu,

and other metals (Huang et al., 2012). Important deposits in the district include the Lamo proximal skarn Zn—Cu deposit, the giant Tongkeng-Changpo and Gaofeng cassiterite-sulfide deposits, and the smaller Huile and Dafulou black shale-hosted tin-base metal deposits. They occur as stratiforms, veins, and stockworks in the Mid-Upper Devonian

* Corresponding authors.

E-mail addresses: suwenchao@vip.gyig.ac.cn (W. Su), pjyju2010@126.com (J. Pan).

carbonate-rich sediments adjacent to the underlying Cretaceous Longxianggai granite pluton (Zhao et al., 2018).

In the past few decades, numerous studies on geology, mineralogy, geochemistry, isotopes, geochronology, and fluid inclusions have been conducted for these deposits in the Dachang district (Chen et al., 1985, 1993; Han and Hutchinson, 1989a, 1989b; Fu et al., 1991, 1993; Zhao et al., 2002, 2007; Pašava et al., 2003; Cai et al., 2004, 2005, 2006a, 2006b; Fan et al., 2004; Wang et al., 2004; Li et al., 2008; Liang et al., 2011; Xu et al., 2011; Wang et al., 2015). Among these, the genesis of the most economically important stratiform-like Sn-polymetallic mineralization has long been debated until recently, centering on a Cretaceous magmatic-hydrothermal genesis (Chen et al., 1993; Fu et al., 1991, 1993; Cai et al., 2005, 2007; Li et al., 2008) or a Devonian submarine exhalation genesis (Cai and Zhang, 1983; Han and Hutchinson, 1989a, 1989b; Han et al., 1997; Jiang et al., 1999; Zhao et al., 2007). These debates existed for long time largely due to lack of convincing chronological data, as mineralization ages were previously determined indirectly via methods such as quartz fluid inclusion Rb–Sr, garnet Sm–Nd, quartz and sanidine Ar–Ar (Wang et al., 2004; Cai et al., 2006a, 2006b; Liang et al., 2011).

Recent application of in situ cassiterite U–Pb dating allows direct determination of tin mineralization age (e.g., Yuan et al., 2008, 2011; Wang et al., 2015; Zhang et al., 2015; Li et al., 2016; Zhang et al., 2017a, 2017b; Guo et al., 2018a, 2018b; Gemmrich et al., 2021; Denholm et al., 2021). Cassiterites from several deposits in the Dachang district have been dated at ca. 90–96 Ma (Wang et al., 2015; Guo et al., 2018a),

providing unambiguous evidence supporting a Cretaceous magmatic-hydrothermal genesis for the stratiform-like Sn mineralization. At the meanwhile, the cassiterite ages imply a genetic association between tin mineralization and the Late Cretaceous intermediate to acid magmatism in the ore field, i.e., the prolonged Longxianggai composite granite (ca. 91 to 97 Ma: Wang et al., 2004; Cai et al., 2006a, 2006b; Liang et al., 2011; Wang et al., 2015; Guo et al., 2018a; Zhao et al., 2018) or the granite and diorite porphyry dikes (ca. 91 Ma: Cai et al., 2006a).

Nevertheless, the existing cassiterite ages are not consistent enough and have a large uncertainty and errors within and between deposits reported by different workers. For example, Wang et al. (2015) reported the LA-MC-ICP-MS cassiterite U–Pb age of 95.8 ± 2.6 Ma for the No. 92 orebody of the Tongkeng deposit, whereas Guo et al. (2018a) reported the LA-ICP-MS cassiterite U–Pb age of 91.5 ± 2.3 Ma for the same orebody. These inconsistent ages with relatively large analytical error may be attributed to the insufficient number of valid measurements and they hamper a direct age comparison with different lithofacies of the Longxianggai granite or the porphyritic dikes to further access their genetic link, especially considering the short-lived magmatic-hydrothermal mineralization process that generally lasts less than 1 m.y (Cathles et al., 1997; Quadt et al., 2011; Li et al., 2022). In this study, massive amount of cassiterite LA-ICP-MS U–Pb data from the Tongkeng and Huile deposits are obtained to precisely determine their mineralization ages with hitherto the best accuracy and precision reported. Our new cassiterite ages together with their trace element compositions provide new constraints on the genesis of the tin mineralization in the

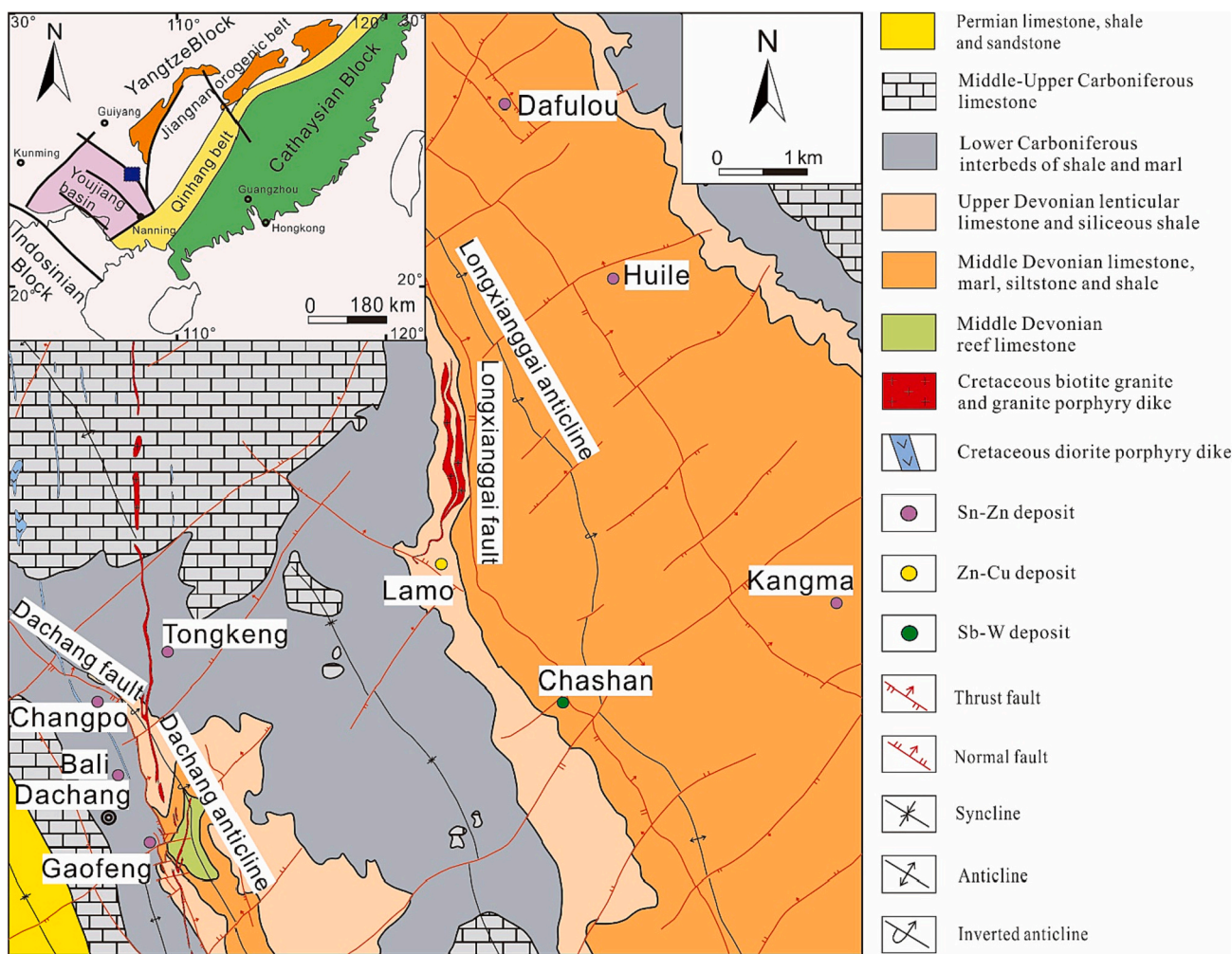


Fig. 1. Geological map of tin-polymetallic deposits in the Dachang district. (Modified from Chen et al., 1993).

Dachang ore field and have implications for the ongoing mineral exploration in the district.

2. Geological setting

The world-class Dachang tin-polymetallic ore field (Fig. 1) is located in the center part of the Danchi fold belt in the Youjiang basin, which is a Devonian-Triassic rift basin on the southwestern margin of South China (Guo et al., 2018a). Sedimentary rocks in the Dachang district consist of Devonian siltstone, black shale, lenticular and reef limestone, Carboniferous limestone and siltstone, and Permian sandstone. The major structural systems include the NW-trending Longxianggai and Dachang anticlines (Fig. 1). The Longxianggai anticline is cut by the Longxianggai reverse fault on the west flank, where the Longxianggai granite intruded. The Dachang anticline is parallel to the main fold and is cut by the Dachang reverse fault and the granitic and diorite porphyry dikes. A series of the NE-trending normal fault cut the anticlines and the reverse faults.

Magmatic rocks exposed in the Dachang district consist of the Longxianggai composite biotite granite and granitic/diorite porphyry dikes (Fig. 1), which were emplaced at 91 ± 1 Ma to 96.6 ± 2.5 Ma and 91 ± 1 Ma (zircon U-Pb ages, Cai et al., 2006a; Liang et al., 2008), respectively. The Longxianggai granite is the main intrusive body in the district, with a small outcropped area of 0.5 km^2 . It is composed of several phases including biotite granite, phenocryst-bearing biotite granite, and porphyritic granite (Cai et al., 2020). Rock-forming minerals include quartz (30–32 vol%), K-feldspar (35–40 vol%), plagioclase (20–25 vol%), biotite (3–6 vol%), and muscovite (1–2 vol%), with accessory ilmenite, zircon, tourmaline, and monazite (Guo et al., 2018a). The granitic porphyry dike has a fine-grained matrix, with variable proportions (15–40 vol%) of medium- to coarse-grained quartz, K-feldspar, and albite phenocrysts. The diorite porphyry dike, parallel to the granite porphyry dike in the east ore section, has a micro- to fine-grained matrix and contains medium-grained plagioclase, quartz, K-feldspar, and biotite phenocrysts.

A variety of styles of tin-polymetallic mineralization in the Dachang district are present, including cassiterite-bearing veins/stockworks ores in the upper part and stratiform Zn—Cu ores in the lower part (e.g. Tongkeng), massive cassiterite-sulfide ore (e.g. Gaofeng), and Zn—Cu skarn ore (e.g. Lamo). All tin mineralization in the Dachang ore field are spatially associated with the Cretaceous Longxianggai granite and the granitic/diorite porphyry dikes.

3. Geology of deposits

Economic deposits in the Dachang ore field (Fig. 1) include the Lamo proximal skarn Zn—Cu and Chashan Sb—W deposit in the central zone, the Tongkeng-Changpo and Gaofeng cassiterite-sulfide deposits in the western zone, and the Huile, Dafulou, and Kangma black shale-hosted tin-polymetallic deposits in the eastern zone.

The Tongkeng deposit is the largest tin-polymetallic deposit in the Dachang district and accounts for 60 % of the Sn reserve, with 0.68 Mt. of Sn, 4.5 Mt. of Zn, and 0.08 Mt. of Cu being verified (Cai et al., 2020). It lies at the northeast limb of the Dachang anticline, approximately 4 km southwest of the exposed Longxianggai granite pluton (Fig. 1). The deposit is hosted in Upper Devonian limestone and siliceous rocks and consists of cassiterite-bearing veins/stocks in the upper part and stratiform Zn—Cu ores in the lower part (Fig. 2). No. 91 and No. 92 orebodies are the two largest producers of Sn in the Dachang district. No. 91 orebody is hosted in banded limestone of the Upper Devonian Wuzhishan Formation and it has a size of 1030 m long, 250 m wide, and 16 m thick, with ore grade averaging at 1.48 % for Sn and 3.05 % for Zn (Cai et al., 2020). No. 92 orebody is hosted in the siliceous rocks of the Upper Devonian Liujiang Formation and it has a size of 1130 m long, 700 m wide, and 26 m thick, with average grade of Sn at 0.8 % and Zn at 2.1 % (Cai et al., 2020). Ore minerals of both No. 91 and No. 92 orebodies consist of cassiterite, pyrrhotite, pyrite, arsenopyrite, sphalerite, marcasite, and various sulfosalts such as jamesonite and boulangerite. According to our field observation and previous studies (Fu et al., 1991; Cai et al., 2007), these minerals can be roughly divided into three

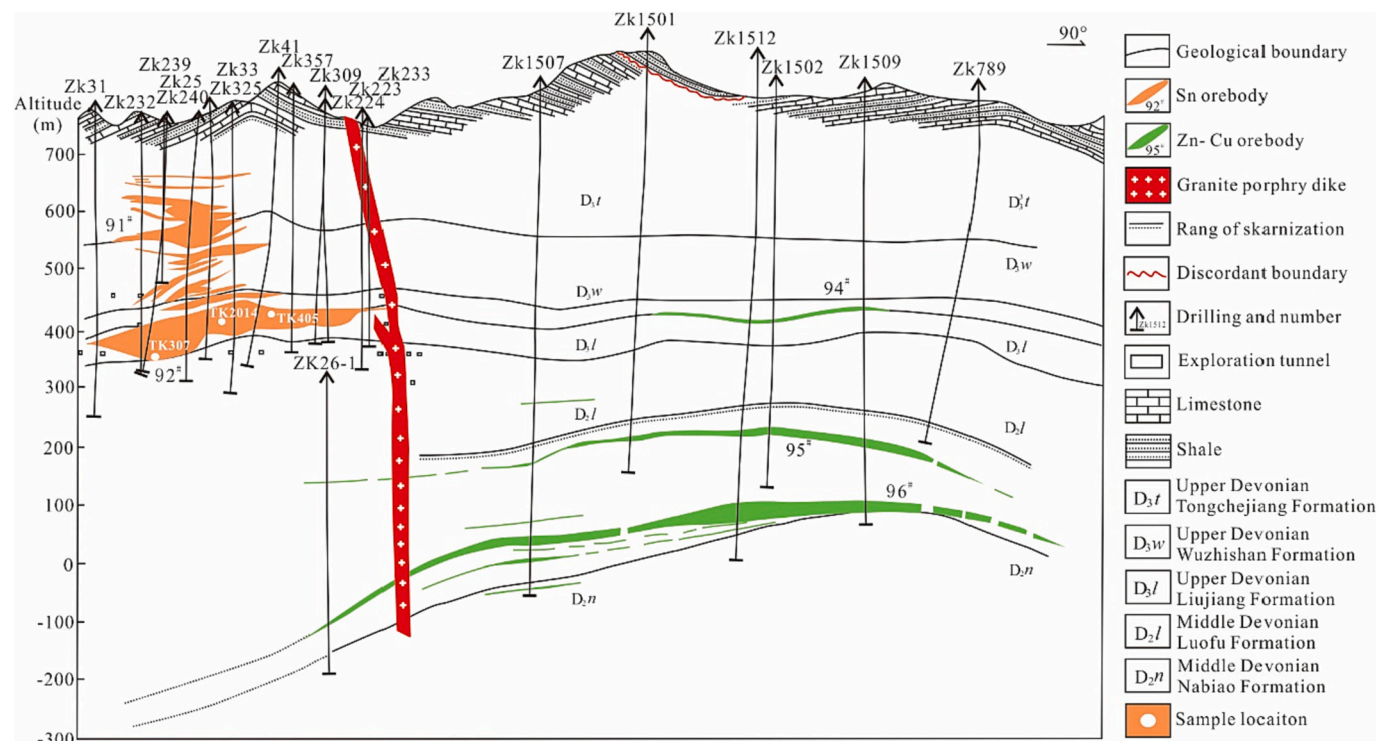


Fig. 2. Cross-section map of the Tongkeng deposit.
(Modified from Liang et al., 2008).

mineralization stages according to the crosscutting relationships and mineral assemblages, including cassiterite - quartz - tourmaline (stage I); cassiterite - arsenopyrite - pyrite - pyrrhotite - sphalerite - quartz (stage II), and galena - stibnite - marcasite - sulfosalt - calcite - quartz (stage III).

Recent exploration drillings (Fig. 2) reveal that three Zn—Cu orebodies (No. 94, 95, and 96) occur in the bottom of the Tongkeng deposit, with proven resource of 2.12 Mt. of Zn and 0.08 Mt. of Cu (Cai et al., 2020). They occur as stratiform shape and are hosted in calcareous mudstone and marl of the Middle Devonian Luofu Formation, and have sizes of 2235–2737 m long, 3.55–5.50 m thick, with grade averaging at 3.04–5.81 % for Zn and 0.13–0.27 % for Cu (Cai et al., 2020). The ore minerals consist mainly of sphalerite, pyrite, pyrrhotite, and chalcopyrite, with a small amount of garnet, wollastonite, tremolite, and chlorite.

The Huile deposit (Fig. 1) lies at the northeast flank of the Longxianggai anticline, approximately 2 km from the exposed Longxianggai granite pluton, and it contains 11,000 t of Sn and 10,000 t of Zn (Xie, 2017; Guo et al., 2018a). The deposit is hosted in the Middle Devonian shale, marl, and siltstone of the Nabiao Formation and the mineralization occurs mainly as cassiterite-bearing quartz veins. Two styles of orebody geometry have been recognized, i.e., stratiform orebodies that are flat-lying, dipping at 15°E, and fault-hosted orebodies that are controlled by NW- and NE-trending high-angle faults (Fig. 3). The ore stage minerals consist of cassiterite, arsenopyrite, pyrrhotite, pyrite, and sphalerite, along with vein quartz and calcite.

4. Samples and analytical methods

Over two hundred ore samples were collected from the Tongkeng and Huile deposits in the Dachang district to look for optimal cassiterite materials used for subsequent isotopic and geochemical determination. Among these, five best preserved cassiterite-bearing samples were analyzed in this study (Figs. 2 and 3). Three samples (TK307, TK2014, and TK405) were collected from No. 92 orebody at 300–400 m mining level in the Tongkeng deposit. They contain cassiterite, arsenopyrite, sphalerite, quartz, and calcite (Fig. 4 A-D). Two samples (HL601-B and HL601-C) were collected from No. 2 orebody at +150 m mining level in the Huile deposit (Fig. 3). They contain cassiterite, arsenopyrite, pyrrhotite, quartz, and calcite (Fig. 4 E-H). The two samples from the Huile were originally collected from the same orebody with several meters in between. They display same texture and mineral assemblage and were thus merged into one sample during analysis. The cassiterite-bearing samples were firstly cut into polished thin sections to check their petrographic features and the crystallization characteristics of the cassiterite. The cassiterite grains from both the Tongkeng and Huile deposits show clear oscillatory growth zoning under transmitted light observation (Fig. 4B, G, H). It is noteworthy that cassiterite grains from the Tongkeng are generally in the size of hundreds of microns to few millimeters, whereas the cassiterite grains from the Huile have much larger sizes up to few centimeters. The rest of the samples were crushed to 40–60 mesh, and cassiterite grains were separated using standard

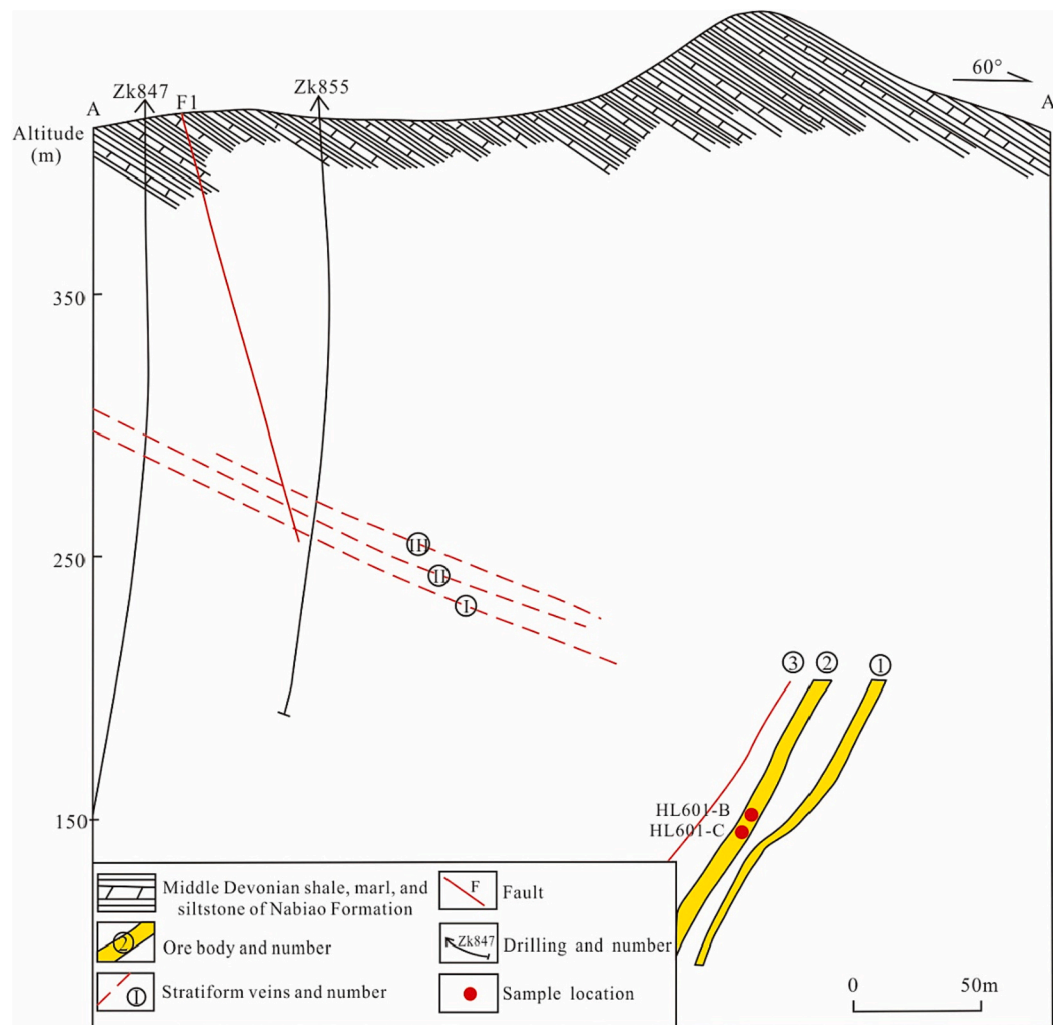


Fig. 3. Cross-section map of the Huile deposit.
(Modified from Xie, 2017).

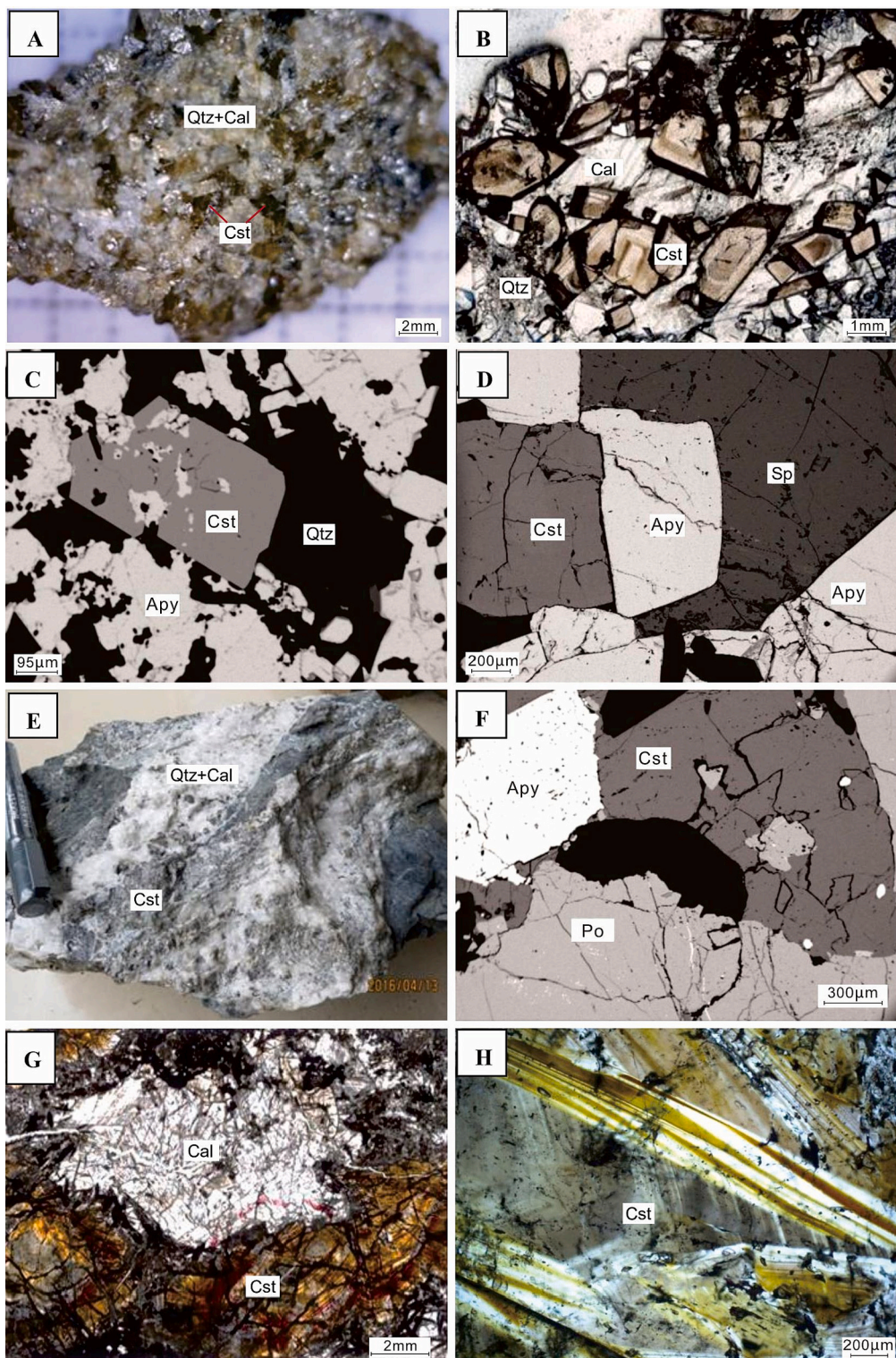


Fig. 4. Representative photographs and photomicrographs of ores from the Tongkeng (A-D) and Huile (E-H) deposits, illustrating the mineral assemblages in the studied samples. Abbreviations: Qtz = quartz; Cal = calcite; Cst = cassiterite; Apy = arsenopyrite; Sp = sphalerite; Po = pyrrhotite.

heavy liquid and magnetic techniques. Then, they were handpicked under a binocular microscope, mounted with external standard in an epoxy resin disc and polished. Based on observations of internal and superficial textures via transmitted light microscope and cathodoluminescence images, inclusion-free cassiterite grains with smooth and homogeneous surface were selected for U—Pb dating and trace element analysis. The trace element data were eventually grouped

according to the color (dark- and light-brown) of cassiterite growth zones where the spot ablation was performed.

In situ cassiterite U—Pb dating and trace elemental analysis were performed at Guizhou Tongwei Analytical Technology Co. Ltd., using a Thermo Fisher iCAP RQ ICP-MS equipped with a Resonetics RESolution S-155 laser ablation system. The holder of the laser system is large (155 mm × 105 mm), which can load 20 mounts at each turn. The

instrumental parameters and operating conditions as well as analytical procedures were similar as those reported by Li et al. (2016) and Guo et al. (2018a), which are summarized below.

Before analysis, the system was optimized using NIST SRM614 ablated with 50 μm spot size and 3 $\mu\text{m}/\text{s}$ scan speed to ensure maximum signal intensity and low oxidation ratio. Helium gas carrying the ablated sample aerosol was mixed with argon (carrier gas) and nitrogen (additional di-atomic gas) to enhance sensitivity, and finally flowed into ICP-MS instrument. Cassiterite grains were analyzed using a laser energy density of 3.0 J/cm^2 , a spot size of 50 μm , and a laser pulse rate of 10 Hz. NIST SRM614 and an in-lab cassiterite AY-4 were used for external elemental and isotopic calibration, respectively. Cassiterite AY-4 was collected from the Anyuan tin deposit of the Furong district, South China, and has been well dated using ID-TIMS with a U—Pb age of 158.2 \pm 0.4 Ma (Yuan et al., 2011). Every five sample spots were followed by one AY-4 analysis and one NIST SRM614 analysis. Each spot analysis incorporated a background acquisition of approximately 15 s, followed by 20 s sample data acquisition. Isotope data were collected in time-resolved mode. For U—Pb isotopic analyses, dwell times for each mass scan are 25 ms for ^{206}Pb , 55 ms for ^{207}Pb , and 15 ms for ^{235}U and ^{238}U , 10 ms for ^{208}Pb , 5 ms for ^{232}Th . ^{118}Sn was used as the internal standard for calibrating the contents of trace elements. Raw data reduction was performed off-line using Iolite 3.0 software (Paton et al., 2011). Tera-Wasserburg U—Pb plots were processed using Isoplot 3.0 (Ludwig, 2003). Data uncertainties of isotopic ratios for individual spots are reported at 2 σ level, and the errors of their weighted mean $^{206}\text{Pb}/^{238}\text{U}$ ages are 2 σ (Li et al., 2016).

5. Results

5.1. Cassiterite U—Pb ages

LA-ICP-MS U—Pb dating results for cassiterite grains from the Tongkeng and Huile deposits are listed in Table 1 and are showed in Fig. 5.

A total of 280 spot data were obtained from the three cassiterites samples (TK307, TK2014, and TK405) of the Tongkeng deposit. These cassiterite generally contain variable contents of U, ranging from 0.12 ppm to 28.80 ppm. On the Tera-Wasserburg plots (Fig. 5A, B, and C), they define regression lines that yielded lower intercept ages of 91.13 \pm 0.61 Ma ($n = 89$, MSWD = 2.2), 89.46 \pm 0.47 Ma ($n = 87$, MSWD = 1.7), and 89.76 \pm 0.44 Ma ($n = 104$, MSWD = 1.5), respectively.

In the Huile deposit, cassiterites also contain variable concentrations of U, ranging from 0.25 ppm to 28.62 ppm. A total of 111 spot analyses for cassiterites is distributed along a well-defined regression line that yielded a lower intercept ages of 89.00 \pm 1.3 Ma ($n = 111$, MSWD = 2.8) (Fig. 5D).

5.2. Trace element compositions of cassiterite

A total of 98 spot analyses for trace elements were measured by LA-ICP-MS on cassiterite bands with different colours (dark- and light-brown, Fig. 4B, G, and H) from the Tongkeng and Huile deposits. The concentrations of trace elements are listed in Table 2 and displayed in Fig. 6.

Cassiterite bands with different colours (Fig. 4B) in the Tongkeng deposit contain high concentrations of Fe (average = 195.20 ppm to 239.78 ppm), W (1532.54 ppm to 1775.05 ppm), Ti (330.68 ppm to 455.44 ppm), Sc (9.28 ppm to 25.66 ppm), Zr (1.47 ppm to 2.23 ppm), Ga (8.97 ppm to 11.44 ppm), and Nb (2.44 ppm to 2.73 ppm) (Table 2, Fig. 6A). In the Huile deposit, cassiterites (Fig. 4G and H) also contain high contents of Fe (average = 4956.64 ppm to 8934.15 ppm), W (150.60 ppm to 2864.78 ppm), Ti (388.78 ppm to 490.82 ppm), Sc (4.35 ppm to 4.61 ppm), Zr (4.17 ppm to 4.53 ppm), Ga (6.28 ppm to 10.74 ppm), and Nb (5.04 ppm to 6.09 ppm) (Table 2, Fig. 6A). In the binary Fe vs. W diagram (Fig. 6B), most cassiterites are plotted in the field of

granite-related tin deposits compiled by Guo et al. (2018b). In all cassiterites, Fe and Nb + Ta have slight negative correlation (Fig. 6C), whereas Fe and Ga, Hf and Zr, and Nb and Ta have positive correlations (Fig. 6D, E and F).

6. Discussion

6.1. Growth environment of cassiterite

Cassiterite has a tetragonal lattice structure, with Sn cations in sixfold coordination with oxygen (Cheng et al., 2019). It can accommodate a wide range of trace elements, including Fe, Ti, W, Nb, Ta, Mn, Ga, and Sc, which substitute for Sn cations (Schneider et al., 1978; Moore and Howie, 1979; Cheng et al., 2019). Previous studies indicated that chemical compositions of cassiterite are effective indicators for its precipitation environment and mineralization type (Möller et al., 1988; Hennigh and Hutchinson, 1999; Guo et al., 2018a, 2018b; Cheng et al., 2019). The Fe and W contents in cassiterite from the granite-related tin deposits are generally different from those of the sedimentary-exhalative (SEDEX) or volcanogenic massive sulfide (VMS) deposits (Fig. 6B), making them an effective factor to differentiate mineralization types (Taylor, 1979; Hennigh and Hutchinson, 1999; Guo et al., 2018a, 2018b). Our LA-ICP-MS trace element spot analyses of cassiterite from the Tongkeng and Huile deposits show broadly similar range of Fe and W contents with previous study (Fig. 6B, Guo et al., 2018a), suggesting a granite-related magmatic hydrothermal environment. Moreover, the Nb + Ta contents of the cassiterite measured from the Tongkeng and Huile deposits are characteristic of skarn-type tin mineralization (Fig. 6C), implying their genetic association with skarn-related magmatic hydrothermal system. Because of the low activities of Nb and Ta in lower temperature fluids, the difference of Nb and Ta contents in cassiterite between different mineralization styles may essentially reflect their temperature condition (Stevens and Taylor, 1973; Murciego et al., 1997). The light-colored cassiterite in both the Tongkeng and Huile deposits generally show higher but restricted Nb and Ta contents compared to dark-colored cassiterite which yields rather broad ranges (Fig. 6F), likely suggesting temperature fluctuation during mineralization.

In cassiterite, Sn^{4+} has a similar ionic radius ($r = 0.69 \text{\AA}$) and charge balance with tetravalent elements such as Ti^{4+} , Zr^{4+} , Hf^{4+} , W^{4+} and U^{4+} , thus allowing direct substitution (Cheng et al., 2019). Because Ga is mainly present as Ga^{3+} in cassiterite and its ionic radius ($r = 0.62 \text{\AA}$) is close to Fe^{3+} ($r = 0.65 \text{\AA}$, Shannon, 1976), the obvious positive correlation between Fe and Ga contents in cassiterite (Fig. 6D) may indicate that Fe is predominantly Fe^{3+} in cassiterite of both the Tongkeng and Huile deposits. Nb and Ta are predominantly pentavalent in cassiterite (Nb^{5+} and Ta^{5+}), and they can substitute for Sn^{4+} by coupling with Fe^{3+} (Plimer et al., 1991; Möller et al., 1988). In this scenario, the molar ratio of Fe/(Nb + Ta) in cassiterite should be near 1, which is clearly not the case for our data (Table 2). The significant excess of Fe over Nb + Ta in cassiterite from the Tongkeng and Huile deposits would thereby indicate other mechanisms to absorb Fe^{3+} , likely being the coupling substitution of $\text{Fe}^{3+} + \text{OH}^- \rightarrow \text{Sn}^{4+} + \text{O}^{2-}$ (Möller et al., 1988; Tindle and Breaks, 1998; Pieczka et al., 2007).

Zr and Hf have similar geochemical properties and therefore Zr/Hf ratios in most geological systems remain constant and are close to 35–40 of chondrite (Hoskin and Schaltegger, 2003). Significant deviation of Zr/Hf ratios in cassiterite between different tin mineralization styles is reported in the giant Gejiu Sn polymetallic deposits (Cheng et al., 2019), and it is explained by preferential mobilization of Zr relative to Hf by hydrothermal fluids enriched in F and B (Rubin et al., 1993). In contrast, the Zr/Hf ratios measured from the Tongkeng and Huile deposits are very consistent round 40 which are close to the chondrite values and most geological systems (Fig. 6E). Our data may suggest that the fluid-derived Zr/Hf fractionation between different tin mineralization styles is not obvious in Dachang. This hypothesis may be geologically

Table 1

LA-ICP-MS U—Pb dating results of cassiterite from the Tongkeng and Huile deposits.

Analysis spot	Isotope ratios					
	U (ppm)	$^{207}\text{Pb}/^{206}\text{Pb}$	$\pm 2\sigma$	$^{207}\text{Pb}/^{235}\text{U}$	$\pm 2\sigma$	$^{206}\text{Pb}/^{238}\text{U}$
<i>TK307</i>						
307-1	9.49	0.0613	0.0041	0.1172	0.0079	0.0147
307-1_1	9.14	0.2340	0.0220	0.6270	0.0730	0.0186
307-1_2	8.32	0.0506	0.0047	0.0976	0.0081	0.0147
307-1_3	8.39	0.0575	0.0049	0.1079	0.0083	0.0147
307-1_4	8.51	0.0525	0.0042	0.0941	0.0078	0.0145
307-1_5	8.71	0.0555	0.0050	0.1046	0.0083	0.0148
307-1_6	6.45	0.3270	0.0200	0.9170	0.0800	0.0224
307-1_7	1.71	0.5910	0.0370	2.4300	0.2700	0.0357
307-1_8	1.22	0.8555	0.0110	139.0000	12.0000	1.2483
307-10	2.16	0.0712	0.0083	0.1050	0.0120	0.0146
307-10_2	3.48	0.0480	0.0052	0.0927	0.0090	0.0138
307-10_3	6.77	0.0534	0.0042	0.1021	0.0081	0.0141
307-10_4	19.62	0.0496	0.0025	0.0914	0.0040	0.0138
307-10_5	18.10	0.0485	0.0025	0.0896	0.0047	0.0142
307-11	7.28	0.3000	0.0280	0.7670	0.0970	0.0204
307-11_1	8.45	0.5730	0.0330	2.5900	0.3700	0.0362
307-11_2	6.56	0.0787	0.0058	0.1460	0.0120	0.0148
307-11_3	9.23	0.1950	0.0130	0.4220	0.0270	0.0173
307-11_4	7.00	0.4630	0.0200	1.4960	0.0770	0.0267
307-11_5	6.48	0.3610	0.0170	1.0970	0.0670	0.0234
307-11_6	8.95	0.2580	0.0310	0.4710	0.0460	0.0200
307-11_7	7.33	0.3480	0.0160	1.0270	0.0760	0.0234
307-12	0.48	0.7760	0.0230	24.9700	0.9800	0.2365
307-12_1	3.21	0.3970	0.0180	1.3090	0.0520	0.0253
307-12_2	4.64	0.0797	0.0064	0.1630	0.0110	0.0146
307-12_3	2.99	0.0739	0.0070	0.1350	0.0140	0.0146
307-12_4	3.15	0.0562	0.0063	0.1030	0.0130	0.0137
307-12_5	4.68	0.0560	0.0056	0.1006	0.0092	0.0144
307-13	6.89	0.0485	0.0044	0.0937	0.0076	0.0141
307-13_1	7.88	0.0448	0.0045	0.0805	0.0070	0.0141
307-13_2	7.34	0.0539	0.0045	0.0989	0.0082	0.0139
307-13_3	6.66	0.0486	0.0042	0.0930	0.0085	0.0145
307-14	5.80	0.6340	0.0190	4.0200	0.2300	0.0473
307-14_1	12.57	0.2670	0.0150	0.6860	0.0410	0.0196
307-15	1.95	0.7100	0.0320	6.6900	0.3900	0.0702
307-15_1	0.21	0.8440	0.0310	39.1000	3.5000	0.3671
307-15_2	0.20	0.5700	0.0590	3.1800	0.5800	0.0506
307-15_3	1.89	0.1230	0.0120	0.2760	0.0260	0.0160
307-15_4	1.00	0.0610	0.0160	0.0910	0.0300	0.0140
307-15_6	0.92	0.0970	0.0150	0.2170	0.0340	0.0155
307-15_7	0.17	0.6150	0.0500	6.2500	0.6900	0.0731
307-15_8	0.51	0.7860	0.0440	11.1100	0.7700	0.1027
307-3	0.44	0.1090	0.0350	0.1810	0.0730	0.0150
307-3_1	1.33	0.0770	0.0130	0.1510	0.0240	0.0156
307-3_2	1.06	0.0620	0.0110	0.1700	0.0280	0.0153
307-4	2.76	0.7530	0.0360	14.2400	0.7100	0.1500
307-4_1	1.83	0.2050	0.0170	0.5280	0.0420	0.0195
307-4_2	11.27	0.2708	0.0084	0.6860	0.0250	0.0200
307-4_4	0.45	0.4050	0.0440	1.3600	0.1400	0.0241
307-4_5	0.92	0.0650	0.0180	0.1070	0.0360	0.0145
307-4_6	3.56	0.5730	0.0200	3.3400	0.1700	0.0441
307-4_7	3.50	0.7020	0.0300	5.9900	0.9000	0.0867
307-5	0.60	0.1810	0.0310	0.4310	0.0860	0.0162
307-5_1	0.42	0.0740	0.0290	0.1640	0.0680	0.0143
307-5_2	0.51	0.0870	0.0320	0.1550	0.0590	0.0147
307-5_4	0.34	0.7260	0.0330	14.0000	2.2000	0.1513
307-5_5	6.38	0.0704	0.0070	0.1320	0.0110	0.0144
307-5_6	3.30	0.0645	0.0068	0.1210	0.0140	0.0145
307-5_7	0.82	0.0570	0.0210	0.0900	0.0370	0.0138
307-6	0.65	0.8590	0.0190	59.9000	3.8000	0.5607
307-6_1	0.24	0.8900	0.0200	288.0000	21.0000	2.3591
307-6_2	3.54	0.8210	0.0170	23.3000	1.7000	0.2285
307-6_3	8.31	0.5430	0.0190	2.1540	0.1000	0.0318
307-7	5.89	0.2920	0.0170	0.6680	0.0370	0.0200
307-7_1	2.20	0.3330	0.0190	0.8690	0.0380	0.0207
307-7_2	0.74	0.0670	0.0220	0.1310	0.0440	0.0149
307-7_3	2.21	0.0468	0.0071	0.0920	0.0140	0.0142
307-7_4	1.81	0.6410	0.0400	4.5200	0.8500	0.0548
307-7_5	2.33	0.0646	0.0090	0.1100	0.0150	0.0137
307-8	10.84	0.0485	0.0031	0.0977	0.0057	0.0144
307-8_1	18.27	0.0518	0.0022	0.0945	0.0043	0.0140
307-8_10	7.08	0.0480	0.0036	0.0907	0.0074	0.0142

(continued on next page)

Table 1 (continued)

Analysis spot	Isotope ratios						
	U (ppm)	$^{207}\text{Pb}/^{206}\text{Pb}$	$\pm 2\sigma$	$^{207}\text{Pb}/^{235}\text{U}$	$\pm 2\sigma$	$^{206}\text{Pb}/^{238}\text{U}$	$\pm 2\sigma$
307-8_11	6.22	0.1370	0.0120	0.2900	0.0280	0.0160	0.0005
307-8_12	28.80	0.2024	0.0075	0.4300	0.0130	0.0175	0.0004
307-8_13	4.92	0.1360	0.0110	0.2970	0.0220	0.0163	0.0005
307-8_14	8.38	0.0508	0.0036	0.0951	0.0064	0.0141	0.0004
307-8_15	8.17	0.0921	0.0093	0.1850	0.0180	0.0149	0.0004
307-8_2	16.61	0.0492	0.0028	0.0898	0.0051	0.0140	0.0003
307-8_3	17.79	0.5176	0.0100	2.3010	0.0810	0.0332	0.0009
307-8_4	15.59	0.0488	0.0033	0.0913	0.0055	0.0142	0.0004
307-8_5	7.32	0.0446	0.0030	0.0828	0.0059	0.0146	0.0005
307-8_6	6.08	0.3730	0.0110	1.1790	0.0340	0.0243	0.0006
307-8_7	6.05	0.0453	0.0047	0.0826	0.0077	0.0145	0.0004
307-8_8	5.69	0.0479	0.0036	0.0924	0.0073	0.0144	0.0005
307-8_9	8.49	0.0515	0.0042	0.0950	0.0071	0.0140	0.0004
307-9	8.59	0.0523	0.0031	0.1049	0.0069	0.0143	0.0004
307-9_1	8.79	0.0497	0.0037	0.0901	0.0074	0.0143	0.0004
307-9_3	5.07	0.0904	0.0065	0.1750	0.0120	0.0152	0.0005
307-9_4	1.42	0.0463	0.0085	0.1250	0.0190	0.0144	0.0010
TK405							
405-1_1	8.53	0.0512	0.0034	0.0931	0.0059	0.0139	0.0004
405-1_2	5.97	0.0433	0.0044	0.0893	0.0095	0.0141	0.0005
405-1_3	7.74	0.0478	0.0034	0.0850	0.0063	0.0137	0.0004
405-1_4	10.30	0.0489	0.0036	0.0933	0.0066	0.0141	0.0005
405-1_5	11.73	0.0474	0.0028	0.0870	0.0048	0.0143	0.0004
405-1_6	11.48	0.0492	0.0030	0.0861	0.0052	0.0139	0.0004
405-10	2.58	0.1090	0.0120	0.1920	0.0220	0.0141	0.0006
405-10_1	0.88	0.1060	0.0170	0.1960	0.0310	0.0153	0.0011
405-10_4	0.20	0.1370	0.0430	0.2690	0.0670	0.0149	0.0011
405-10_6	5.63	0.0516	0.0057	0.0911	0.0088	0.0138	0.0005
405-10_7	4.95	0.0560	0.0056	0.0940	0.0100	0.0142	0.0005
405-10_8	9.13	0.0523	0.0039	0.0919	0.0072	0.0141	0.0004
405-11	1.37	0.0820	0.0130	0.1550	0.0230	0.0146	0.0009
405-11_1	1.45	0.0680	0.0110	0.1360	0.0180	0.0139	0.0008
405-11_2	1.62	0.0770	0.0110	0.1520	0.0220	0.0141	0.0007
405-11_3	0.76	0.0690	0.0200	0.1140	0.0400	0.0151	0.0012
405-11_4	1.18	0.0580	0.0120	0.1120	0.0260	0.0145	0.0010
405-11_5	1.49	0.0635	0.0097	0.1320	0.0210	0.0146	0.0008
405-11_6	1.12	0.0530	0.0170	0.0710	0.0280	0.0129	0.0010
405-11_8	3.80	0.0850	0.0130	0.1380	0.0200	0.0144	0.0005
405-11_9	6.59	0.0581	0.0051	0.1011	0.0079	0.0140	0.0005
405-13	2.64	0.4250	0.0430	1.1100	0.1300	0.0251	0.0019
405-13_1	0.82	0.3120	0.0330	0.6930	0.0850	0.0193	0.0013
405-13_2	14.06	0.0528	0.0032	0.1013	0.0056	0.0140	0.0004
405-13_3	6.60	0.0565	0.0044	0.1032	0.0074	0.0143	0.0005
405-13_4	10.26	0.0510	0.0045	0.0952	0.0079	0.0140	0.0004
405-13_5	10.59	0.0557	0.0036	0.1007	0.0061	0.0142	0.0004
405-13_6	4.94	0.0460	0.0049	0.0934	0.0099	0.0140	0.0006
405-13_7	5.70	0.0572	0.0046	0.0993	0.0083	0.0140	0.0005
405-13_8	5.61	0.0549	0.0064	0.1038	0.0091	0.0136	0.0005
405-13_9	6.80	0.0512	0.0042	0.0939	0.0080	0.0139	0.0005
405-14	2.73	0.5350	0.0290	2.2900	0.2200	0.0365	0.0025
405-14_1	0.92	0.1200	0.0200	0.2240	0.0380	0.0140	0.0009
405-14_2	2.25	0.2040	0.0150	0.4850	0.0270	0.0178	0.0009
405-14_3	0.48	0.8610	0.0220	47.1000	7.0000	0.4443	0.0540
405-14_5	0.46	0.1050	0.0360	0.2080	0.0760	0.0165	0.0015
405-14_6	0.38	0.6590	0.0500	9.2000	1.9000	0.0889	0.0148
405-14_7	0.94	0.0930	0.0150	0.2230	0.0370	0.0159	0.0010
405-15_1	4.77	0.1070	0.0160	0.1750	0.0210	0.0150	0.0009
405-15_2	6.24	0.0529	0.0056	0.0950	0.0110	0.0135	0.0006
405-15_3	9.98	0.0523	0.0039	0.1011	0.0063	0.0145	0.0004
405-15_4	12.76	0.0483	0.0029	0.0885	0.0057	0.0139	0.0004
405-15_5	10.51	0.0564	0.0037	0.0984	0.0063	0.0136	0.0004
405-2_4	6.30	0.0549	0.0045	0.1047	0.0080	0.0140	0.0006
405-2_5	10.65	0.0490	0.0030	0.0874	0.0056	0.0140	0.0004
405-3_1	0.12	0.1370	0.0320	0.2500	0.1000	0.0144	0.0014
405-3_2	0.45	0.0720	0.0180	0.1530	0.0350	0.0162	0.0014
405-3_3	1.19	0.0910	0.0130	0.2000	0.0310	0.0141	0.0010
405-3_4	0.87	0.0800	0.0180	0.1530	0.0460	0.0151	0.0014
405-3_5	4.66	0.0549	0.0051	0.1000	0.0110	0.0145	0.0005
405-3_6	5.41	0.0539	0.0056	0.0989	0.0088	0.0139	0.0005
405-4	4.51	0.2820	0.0150	0.7150	0.0360	0.0200	0.0008
405-4_1	1.14	0.1900	0.0190	0.4620	0.0570	0.0184	0.0010
405-4_2	2.67	0.5000	0.0260	1.9200	0.1300	0.0311	0.0017

(continued on next page)

Table 1 (continued)

Analysis spot	Isotope ratios						
	U (ppm)	$^{207}\text{Pb}/^{206}\text{Pb}$	$\pm 2\sigma$	$^{207}\text{Pb}/^{235}\text{U}$	$\pm 2\sigma$	$^{206}\text{Pb}/^{238}\text{U}$	$\pm 2\sigma$
405-4_3	7.73	0.0549	0.0037	0.1084	0.0066	0.0143	0.0004
405-4_4	7.41	0.0499	0.0041	0.0925	0.0073	0.0141	0.0004
405-4_5	16.61	0.0519	0.0025	0.0956	0.0048	0.0141	0.0003
405-4_6	6.66	0.0600	0.0054	0.1070	0.0110	0.0139	0.0004
405-5	0.18	0.2820	0.0420	0.6200	0.1400	0.0199	0.0023
405-5_1	0.12	0.2780	0.0450	0.7000	0.1300	0.0180	0.0025
405-5_2	0.13	0.0630	0.0260	0.1400	0.1000	0.0141	0.0013
405-5_5	6.45	0.0495	0.0045	0.0899	0.0071	0.0142	0.0004
405-6	8.92	0.0777	0.0049	0.1535	0.0097	0.0146	0.0005
405-6_1	2.82	0.2160	0.0200	0.4920	0.0550	0.0172	0.0009
405-6_2	6.94	0.0624	0.0052	0.1184	0.0088	0.0143	0.0004
405-6_3	8.04	0.0528	0.0044	0.0955	0.0070	0.0142	0.0004
405-6_4	6.75	0.0528	0.0046	0.0967	0.0070	0.0135	0.0005
405-6_5	3.88	0.0520	0.0054	0.1070	0.0110	0.0140	0.0006
405-6_6	8.29	0.0617	0.0050	0.1089	0.0079	0.0139	0.0004
405-6_7	11.71	0.0538	0.0033	0.1015	0.0053	0.0141	0.0004
405-7	13.03	0.5631	0.0094	2.8690	0.0590	0.0396	0.0009
405-7_1	10.11	0.0518	0.0032	0.0960	0.0064	0.0141	0.0004
405-7_2	2.00	0.0847	0.0088	0.1670	0.0150	0.0149	0.0008
405-7_3	11.08	0.0487	0.0031	0.0908	0.0049	0.0142	0.0004
405-7_4	8.46	0.0503	0.0038	0.0947	0.0069	0.0139	0.0004
405-7_5	11.93	0.0690	0.0043	0.1361	0.0077	0.0148	0.0004
405-8	1.38	0.8290	0.0180	43.6000	7.0000	0.3872	0.0582
405-8_1	1.98	0.1160	0.0170	0.2610	0.0400	0.0166	0.0009
405-8_2	1.94	0.7550	0.0200	9.2000	0.7300	0.0963	0.0076
405-8_3	6.64	0.0812	0.0066	0.1550	0.0130	0.0149	0.0005
405-8_4	2.00	0.6200	0.0330	4.0300	0.6600	0.0485	0.0066
405-9	10.87	0.0723	0.0055	0.1410	0.0110	0.0143	0.0004
405-9_1	10.63	0.0606	0.0046	0.1103	0.0077	0.0141	0.0004
405-9_2	13.65	0.0536	0.0032	0.0961	0.0057	0.0140	0.0004
405-9_3	11.78	0.0541	0.0038	0.0993	0.0064	0.0139	0.0004
405-9_4	8.15	0.0578	0.0043	0.1046	0.0077	0.0139	0.0004
405-9_5	6.92	0.0550	0.0049	0.1052	0.0091	0.0141	0.0005
<i>TK2014</i>							
2014	11.59	0.0511	0.0029	0.0986	0.0051	0.0149	0.0004
2014_1	7.54	0.0485	0.0044	0.0934	0.0081	0.0142	0.0004
2014_10	11.90	0.0462	0.0029	0.0852	0.0056	0.0142	0.0004
2014_100	5.19	0.0538	0.0049	0.1012	0.0088	0.0137	0.0005
2014_101	4.77	0.3220	0.0130	0.9260	0.0340	0.0216	0.0007
2014_102	4.21	0.3960	0.0170	1.2430	0.0480	0.0246	0.0009
2014_103	3.00	0.3220	0.0150	0.8580	0.0330	0.0213	0.0008
2014_104	2.10	0.8240	0.0130	28.5000	3.7000	0.2719	0.0339
2014_105	3.06	0.2490	0.0170	0.6340	0.0390	0.0193	0.0007
2014_106	1.08	0.8500	0.0120	72.1000	5.4000	0.6390	0.0529
2014_107	1.60	0.0510	0.0130	0.1190	0.0180	0.0137	0.0009
2014_108	1.48	0.0610	0.0120	0.1270	0.0200	0.0135	0.0007
2014_109	1.19	0.0590	0.0130	0.1440	0.0220	0.0152	0.0009
2014_11	12.14	0.0461	0.0030	0.0869	0.0055	0.0140	0.0004
2014_110	1.90	0.1220	0.0140	0.2480	0.0210	0.0158	0.0007
2014_112	1.54	0.0560	0.0100	0.1240	0.0180	0.0141	0.0008
2014_113	2.03	0.0491	0.0076	0.0980	0.0140	0.0144	0.0007
2014_114	1.84	0.2610	0.0170	0.6750	0.0400	0.0192	0.0008
2014_117	1.06	0.5950	0.0440	3.1800	0.3700	0.0442	0.0039
2014_12	5.47	0.0453	0.0045	0.0816	0.0067	0.0140	0.0005
2014_13	15.57	0.0500	0.0025	0.0925	0.0046	0.0141	0.0003
2014_14	7.67	0.6600	0.0180	5.0200	0.2200	0.0582	0.0022
2014_15	12.59	0.0495	0.0026	0.0920	0.0043	0.0140	0.0003
2014_16	2.78	0.0539	0.0069	0.1060	0.0110	0.0147	0.0006
2014_17	4.36	0.2950	0.0200	0.7180	0.0720	0.0195	0.0008
2014_19	1.02	0.1470	0.0230	0.2950	0.0460	0.0157	0.0011
2014_2	2.51	0.6910	0.0250	4.9600	0.2800	0.0581	0.0028
2014_20	6.57	0.0479	0.0044	0.0894	0.0086	0.0142	0.0005
2014_21	11.77	0.0504	0.0036	0.0917	0.0068	0.0139	0.0004
2014_22	7.85	0.0492	0.0034	0.0859	0.0066	0.0140	0.0004
2014_23	9.71	0.0491	0.0040	0.0888	0.0072	0.0135	0.0004
2014_24	9.97	0.0469	0.0036	0.0846	0.0066	0.0137	0.0003
2014_25	9.88	0.0458	0.0030	0.0860	0.0056	0.0142	0.0004
2014_26	11.84	0.0542	0.0026	0.0948	0.0045	0.0140	0.0004
2014_27	1.39	0.0880	0.0180	0.1710	0.0340	0.0143	0.0009
2014_28	2.50	0.1250	0.0110	0.2310	0.0260	0.0159	0.0007
2014_29	1.58	0.5250	0.0360	2.1300	0.1700	0.0342	0.0019
2014_3	6.67	0.0529	0.0049	0.1006	0.0094	0.0150	0.0005

(continued on next page)

Table 1 (continued)

Analysis spot	Isotope ratios						
	U (ppm)	$^{207}\text{Pb}/^{206}\text{Pb}$	$\pm 2\sigma$	$^{207}\text{Pb}/^{235}\text{U}$	$\pm 2\sigma$	$^{206}\text{Pb}/^{238}\text{U}$	$\pm 2\sigma$
2014_30	1.29	0.4990	0.0330	1.9200	0.1500	0.0299	0.0020
2014_31	1.31	0.5110	0.0320	2.0600	0.1700	0.0316	0.0018
2014_32	1.09	0.3990	0.0340	1.3610	0.0930	0.0257	0.0014
2014_33	0.96	0.5220	0.0450	2.5600	0.2700	0.0383	0.0028
2014_34	0.91	0.6850	0.0320	6.6400	0.5700	0.0735	0.0048
2014_35	1.55	0.1490	0.0240	0.2650	0.0410	0.0161	0.0009
2014_36	1.14	0.0890	0.0160	0.1740	0.0280	0.0152	0.0011
2014_37	1.01	0.0660	0.0160	0.0760	0.0320	0.0141	0.0010
2014_38	5.84	0.0449	0.0043	0.0824	0.0073	0.0138	0.0005
2014_39	6.25	0.0522	0.0054	0.0865	0.0097	0.0141	0.0004
2014_4	0.79	0.0760	0.0190	0.1840	0.0350	0.0147	0.0010
2014_40	11.16	0.0502	0.0033	0.0885	0.0063	0.0139	0.0004
2014_41	11.68	0.0471	0.0028	0.0850	0.0055	0.0139	0.0004
2014_42	11.70	0.0465	0.0034	0.0845	0.0060	0.0140	0.0004
2014_43	8.60	0.0504	0.0037	0.0920	0.0072	0.0141	0.0004
2014_44	10.85	0.0484	0.0031	0.0859	0.0056	0.0140	0.0004
2014_45	4.89	0.3270	0.0160	0.9800	0.0690	0.0225	0.0009
2014_46	3.81	0.2860	0.0190	0.7320	0.0600	0.0197	0.0009
2014_47	1.94	0.1750	0.0220	0.3450	0.0560	0.0168	0.0009
2014_48	1.73	0.0710	0.0120	0.1090	0.0180	0.0136	0.0009
2014_49	5.22	0.0472	0.0041	0.0872	0.0067	0.0136	0.0005
2014_5	6.86	0.0481	0.0040	0.0922	0.0067	0.0143	0.0004
2014_50	6.47	0.0483	0.0041	0.0844	0.0076	0.0140	0.0005
2014_51	8.37	0.0452	0.0035	0.0798	0.0069	0.0135	0.0004
2014_52	12.27	0.0472	0.0030	0.0865	0.0049	0.0138	0.0004
2014_53	10.02	0.0507	0.0035	0.0921	0.0066	0.0139	0.0004
2014_54	9.27	0.0477	0.0035	0.0862	0.0065	0.0138	0.0004
2014_55	8.36	0.0485	0.0037	0.0869	0.0068	0.0139	0.0004
2014_56	4.41	0.0464	0.0056	0.0880	0.0110	0.0137	0.0005
2014_57	3.29	0.4810	0.0240	2.1300	0.1300	0.0335	0.0016
2014_58	3.01	0.4860	0.0190	1.9460	0.0870	0.0308	0.0012
2014_59	2.77	0.3570	0.0180	1.0110	0.0400	0.0223	0.0007
2014_6	12.29	0.0452	0.0027	0.0897	0.0049	0.0142	0.0004
2014_60	2.47	0.3430	0.0140	0.9980	0.0420	0.0212	0.0009
2014_61	1.82	0.2740	0.0160	0.7870	0.0350	0.0197	0.0010
2014_62	1.86	0.1830	0.0160	0.4100	0.0320	0.0161	0.0007
2014_63	2.63	0.0558	0.0083	0.1150	0.0130	0.0145	0.0006
2014_64	9.49	0.0509	0.0033	0.0974	0.0063	0.0141	0.0004
2014_65	10.18	0.0527	0.0034	0.0953	0.0053	0.0139	0.0003
2014_66	6.30	0.0486	0.0044	0.0855	0.0082	0.0140	0.0005
2014_67	5.41	0.0524	0.0049	0.0972	0.0093	0.0138	0.0005
2014_68	4.53	0.0529	0.0052	0.0983	0.0075	0.0141	0.0005
2014_69	3.96	0.7090	0.0210	7.0300	0.2700	0.0726	0.0023
2014_7	8.15	0.0464	0.0033	0.0872	0.0059	0.0143	0.0004
2014_71	1.75	0.0880	0.0130	0.1600	0.0240	0.0151	0.0008
2014_72	1.32	0.1500	0.0230	0.2720	0.0520	0.0155	0.0009
2014_73	1.15	0.2360	0.0170	0.5370	0.0490	0.0175	0.0012
2014_74	1.55	0.0740	0.0120	0.1280	0.0200	0.0147	0.0008
2014_75	1.68	0.0454	0.0076	0.1150	0.0170	0.0141	0.0008
2014_76	1.35	0.0570	0.0130	0.0740	0.0250	0.0137	0.0007
2014_77	1.94	0.0494	0.0084	0.1040	0.0160	0.0139	0.0008
2014_78	2.82	0.0411	0.0062	0.0800	0.0120	0.0139	0.0006
2014_79	3.54	0.0799	0.0080	0.1350	0.0160	0.0143	0.0006
2014_8	8.37	0.0524	0.0043	0.0953	0.0075	0.0140	0.0004
2014_80	3.27	0.7370	0.0230	8.3600	0.4600	0.0849	0.0039
2014_81	0.32	0.8440	0.0180	106.0000	12.0000	0.9838	0.1058
2014_85	0.83	0.7760	0.0420	10.3000	0.5300	0.1039	0.0050
2014_88	2.31	0.4450	0.0230	1.6570	0.0890	0.0278	0.0013
2014_89	3.27	0.2630	0.0170	0.6450	0.0350	0.0193	0.0007
2014_9	7.52	0.0472	0.0035	0.0892	0.0067	0.0145	0.0004
2014_90	3.64	0.2890	0.0160	0.7220	0.0420	0.0194	0.0007
2014_91	4.29	0.4260	0.0170	1.3670	0.0450	0.0246	0.0008
2014_92	2.82	0.3040	0.0180	0.7980	0.0420	0.0203	0.0009
2014_97	1.98	0.0442	0.0083	0.0720	0.0150	0.0139	0.0008
2014_98	5.46	0.0526	0.0044	0.0924	0.0077	0.0140	0.0005
2014_99	4.23	0.0611	0.0055	0.1162	0.0100	0.0140	0.0005
HL601-B							
601-B	3.22	0.7210	0.0180	6.9800	0.3500	0.0749	0.0036
601-B_1	2.28	0.6850	0.0210	5.9700	0.3500	0.0666	0.0034
601-B_12	6.34	0.7700	0.0130	20.3000	2.2000	0.2052	0.0190
601-B_15	7.44	0.3430	0.0530	0.5160	0.0920	0.0188	0.0012
601-B_16	5.47	0.6060	0.0180	3.6500	0.2400	0.0445	0.0019

(continued on next page)

Table 1 (continued)

Analysis spot	Isotope ratios						
	U (ppm)	$^{207}\text{Pb}/^{206}\text{Pb}$	$\pm 2\sigma$	$^{207}\text{Pb}/^{235}\text{U}$	$\pm 2\sigma$	$^{206}\text{Pb}/^{238}\text{U}$	$\pm 2\sigma$
601-B_17	6.63	0.6710	0.0130	5.5100	0.1600	0.0630	0.0019
601-B_18	7.74	0.3190	0.0250	0.8230	0.0680	0.0204	0.0008
601-B_19	7.79	0.5800	0.0210	2.5520	0.0860	0.0353	0.0012
601-B_21	0.91	0.1050	0.0230	0.2220	0.0370	0.0160	0.0012
601-B_22	6.06	0.5390	0.0200	2.3200	0.1200	0.0333	0.0013
601-B_23	7.94	0.6210	0.0220	4.4000	0.3200	0.0520	0.0039
601-B_25	3.60	0.8040	0.0140	22.6100	0.9100	0.2124	0.0086
601-B_26	3.17	0.7750	0.0150	15.8000	1.2000	0.1545	0.0116
601-B_27	11.80	0.7750	0.0140	25.8000	4.0000	0.2306	0.0370
601-B_28	6.36	0.7300	0.0120	9.3900	0.6200	0.0974	0.0056
601-B_30	1.42	0.8050	0.0180	31.4000	4.4000	0.2930	0.0402
601-B_31	2.02	0.7350	0.0190	8.9400	0.7100	0.0985	0.0065
601-B_32	1.89	0.6000	0.0300	3.8600	0.2400	0.0515	0.0020
601-B_34	5.84	0.5310	0.0320	2.2600	0.2100	0.0358	0.0026
601-B_35	0.51	0.8110	0.0210	50.2000	3.2000	0.4686	0.0317
601-B_37	0.45	0.8360	0.0180	39.3000	1.5000	0.3681	0.0159
601-B_38	0.77	0.8070	0.0240	21.2000	2.0000	0.1989	0.0180
601-B_4	1.67	0.7460	0.0180	9.1700	0.7500	0.0924	0.0072
601-B_41	2.66	0.7590	0.0200	11.5000	1.3000	0.1111	0.0116
601-B_43	2.81	0.8100	0.0150	27.0000	2.7000	0.2560	0.0233
601-B_45	4.56	0.8060	0.0140	27.5000	1.8000	0.2592	0.0169
601-B_47	7.93	0.7110	0.0170	8.5000	0.9900	0.0865	0.0094
601-B_48	3.35	0.8000	0.0150	29.7000	3.9000	0.2835	0.0339
601-B_5	1.53	0.3540	0.0280	0.9600	0.1000	0.0222	0.0015
601-B_50	7.56	0.6490	0.0250	3.7200	0.5900	0.0461	0.0049
601-B_52	1.78	0.5180	0.0290	2.0000	0.1600	0.0323	0.0020
601-B_53	0.60	0.7780	0.0420	11.7200	0.5800	0.1114	0.0043
601-B_54	0.40	0.8120	0.0170	103.5000	9.6000	0.9320	0.0931
601-B_55	0.56	0.8190	0.0220	36.8000	3.9000	0.3269	0.0349
601-B_57	5.09	0.3600	0.0180	1.1230	0.0900	0.0224	0.0010
601-B_58	1.70	0.6960	0.0250	9.1000	1.2000	0.0952	0.0116
601-B_59	6.49	0.6980	0.0210	6.1200	0.6400	0.0659	0.0052
601-B_6	2.25	0.7940	0.0170	23.0000	2.4000	0.2190	0.0254
601-B_60	5.50	0.7600	0.0130	14.5000	0.7700	0.1457	0.0084
601-B_61	5.48	0.7140	0.0170	7.0800	0.4400	0.0788	0.0040
601-B_63	2.93	0.6390	0.0220	4.6700	0.4300	0.0543	0.0038
601-B_64	5.89	0.7770	0.0170	12.7300	0.6400	0.1245	0.0067
601-B_65	3.83	0.7650	0.0160	12.6400	0.5200	0.1238	0.0052
601-B_66	4.05	0.7930	0.0150	26.3000	4.1000	0.2475	0.0381
601-B_67	3.31	0.8080	0.0120	26.5000	1.6000	0.2412	0.0127
601-B_69	1.16	0.8040	0.0160	42.2000	3.5000	0.3872	0.0339
601-B_70	5.24	0.7830	0.0140	16.5600	0.8200	0.1653	0.0068
601-B_71	5.25	0.7370	0.0140	10.2600	0.7200	0.1026	0.0067
601-B_72	1.54	0.8331	0.0110	83.0000	6.7000	0.6802	0.0497
601-B_75	7.53	0.7140	0.0200	7.5000	1.1000	0.0745	0.0089
601-B_76	6.68	0.2040	0.0180	0.4380	0.0390	0.0174	0.0006
601-B_77	7.84	0.4000	0.0350	1.1000	0.1600	0.0230	0.0016
601-B_78	10.10	0.1525	0.0072	0.3170	0.0150	0.0166	0.0005
601-B_79	10.68	0.2900	0.0250	0.5780	0.0500	0.0191	0.0007
601-B_8	3.71	0.7100	0.0210	6.8200	0.6400	0.0720	0.0055
601-B_80	5.35	0.2540	0.0160	0.5580	0.0410	0.0181	0.0007
601-B_81	1.96	0.1990	0.0150	0.4120	0.0280	0.0162	0.0009
601-B_82	10.26	0.5600	0.0300	2.6400	0.3100	0.0385	0.0034
601-B_83	0.25	0.2630	0.0410	0.4100	0.1000	0.0177	0.0023
601-B_89	3.85	0.4660	0.0280	1.7100	0.2000	0.0299	0.0016
601-B_9	7.18	0.1213	0.0092	0.2350	0.0190	0.0160	0.0005
601-B_90	1.07	0.5800	0.0380	2.2400	0.2400	0.0368	0.0032
601-B_91	1.72	0.8360	0.0170	37.8000	1.5000	0.3417	0.0127
601-B_94	0.25	0.8260	0.0230	60.2000	6.9000	0.5279	0.0614
601-B_97	8.20	0.7580	0.0150	14.8000	2.5000	0.1481	0.0222
601-B_98	7.48	0.7170	0.0150	7.2400	0.5800	0.0784	0.0051
601-B_99	6.26	0.4540	0.0400	1.5600	0.2600	0.0270	0.0020
<i>HL601-C</i>							
601-C_1	4.33	0.7820	0.0190	9.4900	1.0000	0.0940	0.0084
601-C_16	1.02	0.8240	0.0250	18.0000	1.3000	0.1671	0.0116
601-C_22	0.74	0.8560	0.0160	45.6000	2.2000	0.4062	0.0190
601-C_28	1.53	0.8565	0.0097	217.0000	26.0000	1.9994	0.2433
601-C_29	1.53	0.8140	0.0250	10.9000	1.3000	0.1143	0.0159
601-C_38	0.46	0.8360	0.0360	20.0000	1.5000	0.1830	0.0148
601-C_43	3.23	0.7850	0.0140	16.3700	0.4000	0.1618	0.0048
601-C_44	1.11	0.7230	0.0210	9.4100	0.5000	0.1057	0.0065
601-C_45	1.15	0.0750	0.0120	0.1470	0.0240	0.0141	0.0013

(continued on next page)

Table 1 (continued)

Analysis spot	Isotope ratios						
	U (ppm)	$^{207}\text{Pb}/^{206}\text{Pb}$	$\pm 2\sigma$	$^{207}\text{Pb}/^{235}\text{U}$	$\pm 2\sigma$	$^{206}\text{Pb}/^{238}\text{U}$	$\pm 2\sigma$
601-C_46	6.59	0.7540	0.0150	10.3900	0.5900	0.1060	0.0060
601-C_47	1.92	0.8188	0.0120	33.6000	2.1000	0.3121	0.0190
601-C_49	1.24	0.2130	0.0400	0.4720	0.0870	0.0170	0.0010
601-C_50	2.94	0.4770	0.0500	1.4800	0.2500	0.0285	0.0024
601-C_52	2.89	0.7820	0.0130	15.0500	0.4400	0.1510	0.0053
601-C_54	2.22	0.7820	0.0150	21.1000	1.3000	0.1999	0.0116
601-C_55	1.62	0.6600	0.0240	4.8300	0.4500	0.0575	0.0039
601-C_57	2.61	0.8262	0.0110	48.2000	2.9000	0.4464	0.0254
601-C_58	0.91	0.2870	0.0690	0.6400	0.1200	0.0181	0.0019
601-C_60	0.74	0.7290	0.0400	8.7300	0.5100	0.0934	0.0068
601-C_61	0.79	0.2480	0.0310	0.5360	0.0570	0.0175	0.0014
601-C_62	3.35	0.1310	0.0120	0.2600	0.0230	0.0157	0.0007
601-C_63	1.38	0.8310	0.0130	69.9000	9.3000	0.6284	0.0804
601-C_65	28.62	0.2974	0.0099	0.7440	0.0290	0.0203	0.0005
601-C_66	7.56	0.7841	0.0110	14.2400	0.6800	0.1417	0.0072
601-C_71	4.34	0.6920	0.0140	6.1000	0.2200	0.0686	0.0025
601-C_72	0.59	0.8371	0.0120	87.2000	5.2000	0.8029	0.0455
601-C_74	3.30	0.6030	0.0270	5.3300	0.6400	0.0588	0.0059
601-C_75	0.31	0.8470	0.0150	183.0000	11.0000	1.6556	0.0910
601-C_76	18.60	0.2140	0.0260	0.3780	0.0420	0.0175	0.0007
601-C_77	15.06	0.5750	0.0240	2.7800	0.3800	0.0389	0.0033
601-C_78	8.43	0.4280	0.0180	1.3130	0.0850	0.0247	0.0009
601-C_79	8.45	0.7010	0.0190	5.1500	0.5500	0.0579	0.0050
601-C_80	6.20	0.7670	0.0160	12.6800	0.5300	0.1249	0.0051
601-C_81	3.58	0.6620	0.0230	5.0100	0.2200	0.0597	0.0023
601-C_82	16.43	0.5944	0.0091	3.4570	0.1000	0.0446	0.0013
601-C_83	27.75	0.0683	0.0032	0.1279	0.0058	0.0145	0.0003
601-C_84	7.48	0.0707	0.0053	0.1281	0.0097	0.0144	0.0004
601-C_85	22.81	0.2740	0.0170	0.6850	0.0590	0.0195	0.0006
601-C_87	0.26	0.8420	0.0180	128.0000	11.0000	1.1552	0.0973
601-C_90	0.77	0.8060	0.0190	24.1000	1.1000	0.2235	0.0100
601-C_96	0.92	0.8010	0.0210	22.9000	1.7000	0.2169	0.0159
601-C_97	21.96	0.4790	0.0250	2.1400	0.2400	0.0342	0.0022
601-C_98	17.51	0.4240	0.0170	1.3940	0.0950	0.0248	0.0009
601-C_99	3.47	0.6570	0.0170	5.2600	0.2800	0.0584	0.0029

reasonable given the major tin mineralization style in both the Tongkeng and Huile are rather monotonic compared to the Gejiu tin orefield.

6.2. Timing of tin mineralization in the Dachang district

Various radiogenic isotopic dating methods have been used to constrain the ages of ore-related magmatism in the Dachang district. Cai et al. (2006a) used SHRIMP zircon U–Pb dating on the intrusions and yielded emplacement ages of 91 ± 0.8 to 93 ± 1 Ma for the Longxianggai granite, and 91 ± 0.7 Ma and 91 ± 0.8 Ma for the granite and diorite porphyry dikes, respectively. Liang et al. (2011) reported precise but slightly older and prolonged ages for the Longxianggai granite, ranging from 93.9 ± 0.8 Ma to 96.6 ± 2.5 Ma, measured by LA-MC-ICP-MS zircon U–Pb dating method. The prolonged ages are attributed to the multiple-intruded phases of the Longxianggai granitic pluton (Liang et al., 2011). These ages represent the timing of granitic magmatism in the Dachang district.

Several attempts have been made to date the tin-polymetallic deposits in the Dachang district. Wang et al. (2004) reported two $^{40}\text{Ar}/^{39}\text{Ar}$ ages of 94.5 ± 0.3 Ma on quartz and 91.4 ± 2.9 Ma on sanidine from the No. 91 orebody in the Tongkeng deposit, and an $^{40}\text{Ar}/^{39}\text{Ar}$ age of 94.6 ± 0.5 Ma on quartz from the No. 100 orebody in the Gaofeng deposit, which were interpreted as the age of tin mineralization in the Dachang district. However, the reported $^{40}\text{Ar}/^{39}\text{Ar}$ ages are not adequately reliable because they have irregular age spectrum (Wang et al., 2004). Rb–Sr method for fluid inclusion in quartz was applied to the No. 92 orebody of the Tongkeng deposit and yielded the Rb–Sr isochron age of 93.4 ± 7.9 Ma (Cai et al., 2006b). Aside from doubts on the reliability of the dating methods (e.g., Pettke and Diamond, 1995), the large analytical error on these results have ruled out their usefulness.

Recently, cassiterites from several Sn deposits in the Dachang district

have been dated using the LA-MC-ICP-MS and LA-ICP-MS U–Pb methods. Wang et al. (2015) reported the LA-MC-ICP-MS cassiterite U–Pb age of 95.8 ± 2.6 Ma for the No. 92 orebody of the Tongkeng deposit, whereas Guo et al. (2018a) obtained the LA-ICP-MS cassiterite U–Pb age of 91.5 ± 2.3 Ma for the same orebody. Cassiterites from other deposits in the Dachang district yielded a ca. 3 m.y. range of ages with large errors (Guo et al., 2018a), namely: Gaofeng at 91.2 ± 1.8 Ma, Dafulou at 91.3 ± 7.3 Ma, Huile at 94.5 ± 5.0 Ma, and Kangma at 92.8 ± 4.6 Ma. These ages provide a general time constraint on the tin mineralization and are more reliable than previous $^{40}\text{Ar}/^{39}\text{Ar}$ and Rb–Sr ages in terms of methodology, even though the results are roughly the same. Nevertheless, these cassiterite U–Pb ages are not in good consistency and have a large uncertainty and errors within and between deposits reported by different workers. This variation is caused probably because the number of valid measurements on cassiterite grains from each deposit is insufficient. As exemplified by the data reported by Guo et al. (2018a), only 16 spots were measured for Tongkeng, 9 spots for Dafulou, 7 spots for Huile and 12 spots for Kangma, which resulted in relatively large errors on their concordia and weighted mean ages.

In this study, near 400 cassiterite LA-ICP-MS U–Pb data were obtained from the Tongkeng and Huile deposits to precisely determine their mineralization ages. Our new U–Pb data have narrowed down the mineralization ages of the Tongkeng and Huile deposits to the range of 91 to 89 Ma with hitherto the best accuracy and precision reported, which agrees well with previously published Re–Os age of 90.0 ± 1.1 Ma for molybdenite from the Lamo Zn–Cu deposit in the Dachang district (Zhao et al., 2018). In the other districts in the Danchi metallogenic belt (Fig. 7A), our new ages also overlap with the U–Pb ages of cassiterites from the other deposits: the Zn–Sn deposit in the Mangchang district at 88.4 ± 1.3 Ma (Liao et al., unpublished data), the

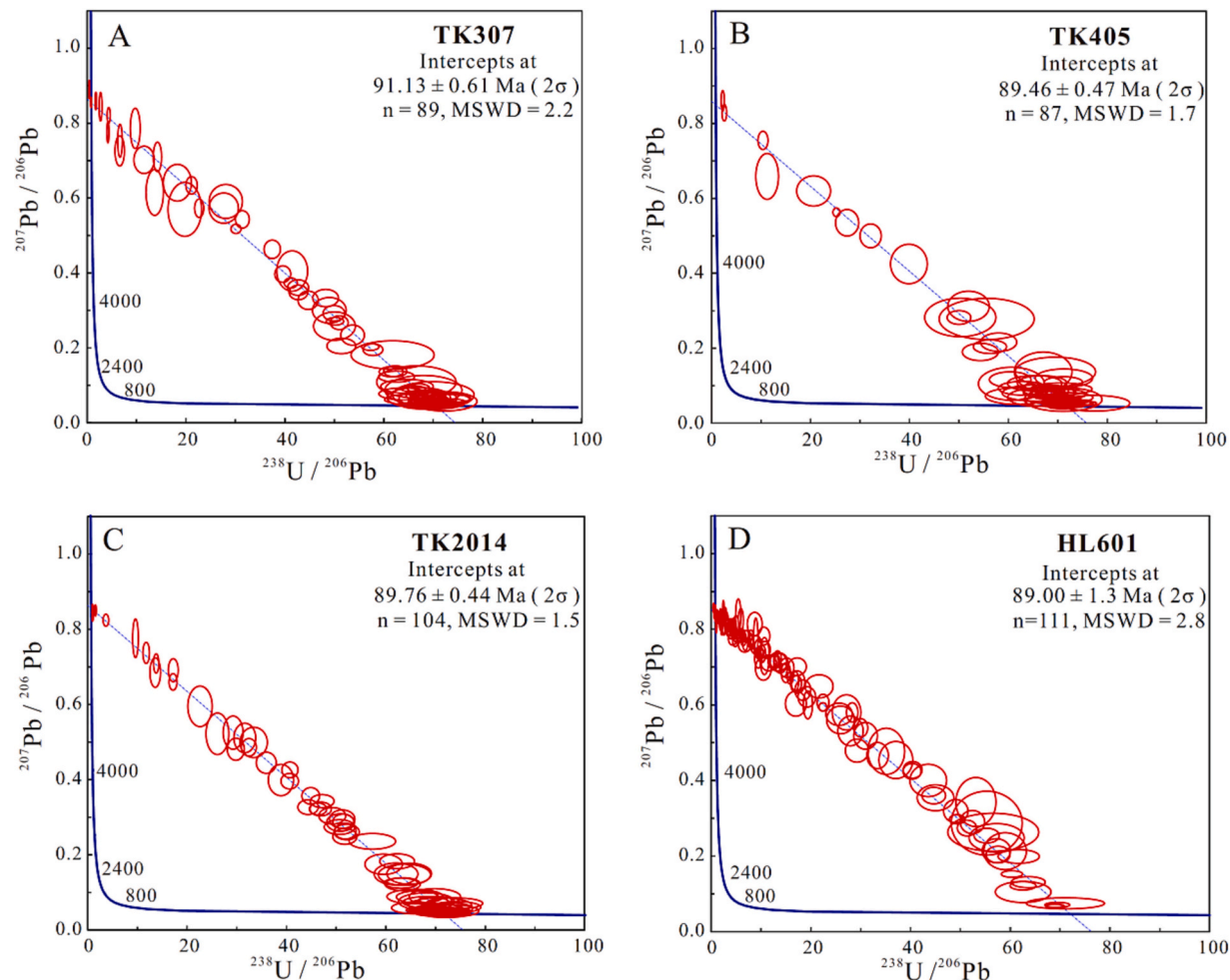


Fig. 5. Tera-Wasserburg U—Pb plots for cassiterites from the Tongkeng (A-C) and Huile (D) deposits in the Dachang district.

Beixiang Sb-Pb-Zn-Sn deposit at 90.6 ± 4.5 Ma (Wu et al., 2022), the Jiangzhupo and Bawang Sb-Zn-Sn deposits in the Wuxu district at 90.2 ± 3.1 Ma and 90.6 ± 4.6 Ma (Xiao et al., 2022), respectively.

In summary, the timing of tin mineralization in the whole Dachi metallogenic belt are all together peaking at 90 Ma (Fig. 7A). This age is consistent with the emplacement ages of 91 Ma for the last porphyritic phase of the Longxianggai granite and the granite/diorite porphyry dikes in the Dachang district (Cai et al., 2006a), and it is also coeval with the granite porphyry dike of 89.1 ± 0.9 Ma in the Mangchang district (LA-ICP-MS zircon U-Pb: Wu et al., 2020), suggesting that the tin mineralization in the belt was most likely formed in intimate association with these granitic porphyritic phases.

6.3. Magmatic affinity of tin mineralization in the Dachang district

How long a hydrothermal system can be sustained by single intrusive event is fundamental to understanding ore formation and establishing genetic models for ore exploration. Thermodynamic calculations showed that a single intrusive event could sustain a hydrothermal system for about 0.8 m.y. under the most favorable conditions (Cathles et al., 1997). High-precision U—Pb ages of individual zircon crystal indicated that the hydrothermal system associated with the porphyry intrusion could have a maximum life span of a few tens of thousands of years (Quadt et al., 2011; Chiaradia et al., 2012), and a maximum time gap of 1 to 0.5 m.y. between the two hydrothermal events would already indicate discrete magmatic-hydrothermal systems (e.g., Muntean and Einaudi, 2001; Bendezú et al., 2003; Pan et al., 2019). The long-lived

hydrothermal activity (~1 m.y.) generally attributes to multiple pulses of intrusion with associated pulses of hydrothermal circulation (Cathles et al., 1997).

Based on previously reported cassiterite U—Pb ages (90–96 Ma), the tin-polymetallic mineralization in the Dachang district is consequently thought to be genetically related to the prolonged Longxianggai granite pluton (93–97 Ma, Liang et al., 2011) given that their ages are overlapping within analytical error (Guo et al., 2018a). Nevertheless, the analytical error of the previously reported cassiterite ages are too large to provide a precise comparison. Taking the 2σ error into account, our new cassiterite ages are apparently younger than the major equigranular phase of the Longxianggai pluton (93–97 Ma, Cai et al., 2006a; Liang et al., 2011) with an absolute time gap of over 2 m.y. However, the mineralization ages are consistent with the latest porphyritic phase of the Longxianggai granite (91 ± 0.76 Ma, Cai et al., 2006a) and the emplacement of granitic/diorite porphyry dikes (91 ± 0.7 Ma to 91 ± 0.8 Ma, Cai et al., 2006a). This suggests that the tin-polymetallic deposits in the Dachang district were most likely formed in magmatic hydrothermal system related to the later, higher evolved granitic phases, rather than the dominated early crystallized equigranular phase of the Longxianggai pluton. This suggestion is also supported by field relationship that the granitic porphyry dike has closer spatial affinity with the massive cassiterite-sulfide orebodies in the giant Tongkeng and Gaofeng deposits (Fig. 1). This affinity is also supported by other districts in the Danchi metallogenic belt. For example, in the Mangchang district (~20 km away from the Dachang district, Fig. 7A), the granitic porphyry dike is the only outcropped intrusion with zircon U—Pb age of

Table 2

LA-ICP-MS trace element compositions of cassiterite from the Tongkeng and Huile deposits.

Analysis spot	Fe	W	Nb	Ta	Zr	Hf	Ti	Sc	Ga
Dark brown cassiterites from Tongkeng deposit									
307_1	236.40	4590.00	0.10	bdl	0.01	bdl	9.26	0.26	8.53
307_2	69.10	2526.00	0.12	bdl	bdl	28.90	0.14	2.22	
307_3	64.60	1989.60	1.92	0.01	0.33	bdl	295.90	1.26	2.17
307_3_3	234.60	2.54	9.23	0.02	6.70	0.20	1649.00	105.98	5.44
307_3_4	280.20	43.50	0.82	0.01	1.03	0.02	805.00	58.30	8.96
307_3_5	541.00	24.46	12.62	bdl	0.11	bdl	493.00	201.40	14.38
307_4	1470.00	604.00	0.63	bdl	0.05	bdl	85.50	57.40	31.59
307_5	496.00	1.33	0.03	bdl	0.25	0.01	118.00	4.12	12.90
307_9	97.10	3086.00	0.80	bdl	0.15	bdl	154.60	0.63	2.86
307_9_2	725.90	238.84	0.40	0.01	0.93	0.03	142.40	23.99	15.98
307_9_4	20.70	218.74	3.90	0.01	0.16	bdl	147.60	4.82	0.78
307_9_5	190.90	3189.00	12.82	0.06	0.47	0.01	218.50	4.84	8.21
307_9_6	204.80	1106.60	0.02	bdl	0.01	bdl	4.37	0.50	9.76
405_2	553.00	8.30	0.44	bdl	0.53	0.02	179.30	21.48	25.01
405_2_1	264.30	346.40	0.90	0.01	1.27	0.04	617.00	14.33	10.99
405_2_2	447.00	2.99	0.12	bdl	bdl	102.10	13.27	16.05	
405_2_3	149.80	2369.00	0.22	bdl	0.13	bdl	238.20	4.71	6.69
405_4_1	548.00	1.21	2.49	0.11	7.60	0.24	940.00	105.00	19.53
405_4_2	80.10	4651.00	5.61	bdl	0.19	bdl	1005.00	3.65	4.58
405_4_3	172.00	271.00	0.04	bdl	0.54	0.01	98.00	4.80	8.60
405_4_4	71.90	2371.00	2.43	0.01	0.45	0.01	107.10	3.37	2.97
405_4_5	125.00	2266.00	3.26	0.06	2.31	0.06	472.00	15.40	6.29
405_4_6	111.00	1236.00	1.08	0.01	0.22	0.01	54.20	1.40	4.31
405_6	391.00	121.60	4.68	0.20	14.71	0.44	3046.00	91.00	18.62
405_6_2	113.10	451.00	0.09	bdl	0.07	bdl	164.00	3.09	5.86
405_6_3	26.80	3306.00	3.90	0.01	0.61	0.01	256.40	12.70	1.34
405_6_5	119.00	369.00	4.62	0.25	28.93	0.97	2263.00	99.30	4.92
2014_1	232.90	425.70	2.81	0.11	8.82	0.28	1297.00	32.42	11.68
2014_1_3	91.70	341.70	1.55	bdl	0.69	0.01	492.00	39.09	4.36
2014_1_6	52.00	4400.00	3.60	bdl	0.13	bdl	400.50	21.26	2.72
2014_1_8	24.50	280.00	bdl	bdl	bdl	0.08	0.01	2.91	
2014_1_9	101.00	3640.00	0.75	bdl	0.02	bdl	219.30	1.75	4.73
2014_2	249.10	1337.00	1.12	0.01	1.74	0.05	393.30	17.80	16.40
2014_2_1	85.60	1579.30	0.03	bdl	0.20	bdl	19.04	0.39	6.41
2014_2_2	99.30	3722.50	2.70	bdl	0.10	bdl	475.40	6.45	5.94
2014_2_3	464.00	143.00	0.04	bdl	1.44	0.03	107.50	9.30	24.10
2014_2_4	101.60	4.20	0.38	bdl	1.00	0.01	785.00	10.00	4.28
2014_2_5	326.00	3700.00	0.31	0.01	1.01	0.03	137.80	29.20	15.85
2014_2_6	121.80	3570.00	0.08	bdl	0.01	bdl	105.60	12.13	5.01
2014_2_7	42.40	2857.60	10.21	0.07	1.87	0.06	446.30	12.04	2.23
2014_2_8	35.90	1442.00	0.56	bdl	0.01	bdl	100.00	3.00	1.66
Average	239.78	1532.54	2.44	0.05	2.23	0.12	455.44	25.66	8.97
Light brown cassiterites from Tongkeng deposit									
307_3	483.00	2.80	0.08	bdl	0.17	bdl	111.50	4.20	11.46
307_3_1	136.20	1.47	0.02	bdl	0.24	0.01	44.30	14.13	4.30
307_3_2	269.60	2.81	0.01	bdl	0.23	bdl	6.56	4.57	7.61
307_6	113.40	1306.00	5.13	0.09	0.94	0.02	486.60	1.79	2.52
307_7	72.60	2734.00	0.50	bdl	0.12	bdl	133.90	1.29	2.38
307_9_1	83.70	1732.00	13.02	0.29	2.98	0.07	1136.50	3.73	1.42
307_9_3	52.10	1874.00	1.03	bdl	0.19	bdl	182.00	0.24	2.15
405_1	116.00	2406.00	1.14	0.01	1.26	0.03	498.90	14.47	5.44
405_1_1	84.80	3455.00	7.00	0.18	6.99	0.24	827.00	23.30	4.23
405_1_2	43.70	3232.00	14.03	0.11	2.82	0.07	622.70	11.62	2.32
405_4	552.00	237.00	0.22	bdl	0.53	0.01	240.20	20.34	25.45
405_6_1	195.10	2312.00	0.02	bdl	bdl	bdl	1.13	bdl	10.50
405_6_4	85.50	6530.00	0.32	bdl	0.07	bdl	75.50	3.18	5.47
2014_1_1	622.90	442.00	2.87	0.08	5.52	0.18	1062.00	35.91	28.36
2014_1_2	117.40	1883.00	0.81	bdl	0.45	0.01	398.80	8.92	6.01
2014_1_4	321.80	673.00	0.04	bdl	0.37	0.01	88.80	1.50	42.92
2014_1_5	17.10	2228.00	2.82	0.03	1.72	0.05	308.80	8.08	0.59
2014_1_7	130.30	2379.00	bdl	bdl	bdl	0.69	bdl	25.92	
2014_2_9	211.60	295.90	0.09	bdl	0.31	0.01	57.00	0.42	28.27
Average	195.20	1775.05	2.73	0.11	1.47	0.06	330.68	9.28	11.44
Dark brown cassiterites from Huile deposit									
601-B_4	98.00	5081.00	1.04	bdl	0.12	bdl	519.90	2.49	0.86
601-B_5	230.00	6980.00	0.42	bdl	0.10	bdl	125.80	2.13	1.14
601-B_6	282.90	7480.00	0.25	bdl	0.06	bdl	86.20	3.40	2.03
601-B_7	176.00	5420.00	22.81	0.07	1.86	0.04	567.30	2.77	1.16
601-B_8	157.20	5630.00	1.46	bdl	0.31	0.01	258.80	4.79	1.17
601-B_9	113.80	4846.00	3.00	bdl	0.06	bdl	531.60	1.09	0.86

(continued on next page)

Table 2 (continued)

Analysis spot	Fe	W	Nb	Ta	Zr	Hf	Ti	Sc	Ga
601-B_10	728.00	1040.00	1.08	bdl	0.27	0.01	329.40	11.01	7.65
601-B_11	373.10	7576.00	0.42	bdl	0.09	0.01	84.00	0.90	4.41
601-B_12	617.00	11,750.00	1.19	bdl	0.09	bdl	194.30	2.41	4.10
601-B_13	345.00	6810.00	1.10	0.01	0.08	bdl	143.10	1.08	1.92
601-B_14	107.70	5902.00	0.46	bdl	0.09	bdl	162.70	0.39	1.22
601-B_15	660.00	4793.00	0.65	0.01	0.14	bdl	178.20	4.52	8.09
601-B_16	902.00	358.00	0.65	0.01	0.56	0.02	339.20	9.89	9.29
601-B_17	265.00	4006.00	22.48	0.09	1.95	0.03	621.00	2.86	1.16
601-B_18	238.10	219.90	0.65	bdl	2.02	0.04	954.00	4.67	3.02
601-B_19	1110.00	93.00	0.23	0.01	0.86	0.02	385.40	9.39	4.03
601-C	268.30	951.00	19.73	0.45	18.74	0.37	2116.00	2.89	0.45
601-C_1	412.20	18.75	1.93	0.20	1.25	0.05	559.00	5.00	2.80
601-C_2	237.00	269.00	18.14	0.15	15.64	0.31	1258.00	2.27	0.49
601-C_3	477.00	174.50	13.63	0.12	17.91	0.34	1763.00	2.98	0.72
601-C_4	98.70	25.40	3.13	0.09	4.01	0.09	316.00	7.56	0.45
601-C_5	163.60	432.80	20.41	0.57	31.34	0.80	834.00	2.25	0.26
601-C_9	364.40	195.00	13.01	0.87	12.31	0.33	727.00	3.01	2.70
601-C_10	390.80	162.00	10.33	0.18	5.22	0.11	661.00	6.33	3.67
601-C_14	17,450.00	0.18	0.01	bdl	0.09	0.01	6.65	4.85	27.11
601-C_16	66,000.00	0.15	0.01	bdl	0.09	bdl	5.74	12.11	32.30
601-C_17	28,500.00	0.04	bdl	bdl	0.05	bdl	6.82	4.46	34.10
601-C_18	18,020.00	0.02	bdl	bdl	1.39	0.04	8.73	4.21	18.77
Average	4956.64	2864.78	6.09	0.20	4.17	0.15	490.82	4.35	6.28
Light brown cassiterites from Huile deposit									
601-B	417.00	86.60	1.56	bdl	0.33	0.01	165.30	1.51	5.14
601-B_1	454.00	81.20	1.37	bdl	0.42	0.01	295.10	2.47	6.91
601-B_2	742.00	780.00	1.42	bdl	0.29	0.01	184.80	1.95	13.39
601-B_3	543.00	55.08	0.32	bdl	0.10	bdl	279.40	14.36	5.70
601-C_6	195.80	41.74	12.12	0.13	20.82	0.45	1805.00	4.21	0.36
601-C_7	214.90	87.30	4.46	0.06	9.80	0.20	547.00	1.92	0.55
601-C_8	244.80	374.00	14.04	0.31	13.27	0.31	599.00	1.74	0.41
601-C_12	18,330.00	0.03	bdl	bdl	0.17	0.01	3.20	2.82	20.85
601-C_13	50,100.00	0.06	bdl	bdl	0.09	bdl	7.10	11.04	39.80
601-C_19	18,100.00	0.02	bdl	bdl	0.02	bdl	1.90	4.07	14.32
Average	8934.15	150.60	5.04	0.17	4.53	0.14	388.78	4.61	10.74

bdl: Below the detection limit.

89.1 ± 0.9 Ma (Wu et al., 2020), which is similar to the cassiterite U—Pb age of 88.4 ± 1.3 Ma for the deposit (Liao et al., unpublished data).

Notably, despite the granitic porphyry dikes are observed as post-ore intrusion by crosscutting massive cassiterite-sulfide orebodies at the Tongkeng and Gaofeng deposits, their ages are indistinguishable from mineralization within the current analytical precision. This implies that the granitic porphyry dikes are probably a slightly later phase of the unrevealed “true” parental granite which may be a discrete episode of intrusion or evolved counterpart of the Longxianggai pluton. In any cases, the multiple magmatic events spanning from the Longxianggai granite to the granitic porphyry dike may be related to successive magma recharge from the same lower crust magma chamber, even though upper-crustal events are discernibly separate.

Late-Cretaceous granite and the related tin-polymetallic deposits also occur along the southern margin of the Youjiang basin, including the world-class Gejiu Sn—Cu, the Dulong Sn—Zn, and the Bainiuchang Sn-Pb-Zn-Ag deposits (Fig. 7C). However, the tectonic model for tin-polymetallic mineralization in the Youjiang basin remains controversial. Many studies have proposed that the Sn ore deposits in the Youjiang basin and northern Vietnam were caused by subduction and slab rollback of the Paleo-Pacific Plate during Cretaceous (Cheng et al., 2016; Mao et al., 2008, 2011; Roger et al., 2012; Zhang et al., 2018a, 2018b). This model explains the linear NNE-SSW trending Cretaceous igneous belt and the related deposits in the coastal area of southeast China (Li et al., 2014; Sun et al., 2007). However, it is difficult to explain an E-W trending Cretaceous magmatic belt and the related Cu and Sn ore deposits from western Guangdong, through the Youjiang basin, to eastern Myanmar (Fig. 7B, C), which is better interpreted as the result of subduction and slab rollback of the Neo-Tethys Plate (Ma et al., 2013; Cao et al., 2016; Gardiner et al., 2016; Sun, 2016; Zhang et al., 2017a,

2017b, 2017c, 2017d, 2018a, 2018b, 2019; Huang et al., 2019).

6.4. Implications for ore exploration

Our new cassiterite U—Pb data demonstrate that the tin-polymetallic mineralization in the Dachang district has a close temporal relationship to the porphyritic granite represented either by the latest phase of the Longxianggai granite or the granite porphyry dikes, with the occurrences of the latter are spatially consistent with the distribution of giant deposits such as the Tongkeng and Gaofeng in the west zone of the Dachang district (Fig. 1). Recent underground mining and drilling projects in the Gaofeng deposit (No. 100 orebody) reveal that the granite porphyry dike extends to ~380 m level and has a depth of at least 1060 m below the present surface where its pluton is not intercepted yet. Although these dikes are post-ore, field observations showed that the porphyry dikes are intimately associated with the massive cassiterite-sulfide orebodies and they are both controlled by the same fault systems (Zhao, 2018; Zhao et al., 2018), implying a close affinity between the tin mineralization and these dikes’ deep concealed counterpart granite of probably slightly earlier emplacement ages. This assumption is also supported by the geochronology data from the Gaofeng deposit where the ages of cassiterite-sulfide ore and the porphyry dikes were both dated at ca. 91 Ma (Guo et al., 2018a; Cai et al., 2006a).

In the Tongkeng deposit, similar spatial and temporal relationships exist between the granite porphyry dikes and the cassiterite-sulfide orebodies except that the horizontal extension of the orebodies are mainly controlled by the host sedimentary strata (Fig. 2). The tin-polymetallic orebodies at Tongkeng are generally restricted above the +300 m level and are several hundred meters away from the deeply concealed granite (Zhao, 2018). The formation of such giant Sn

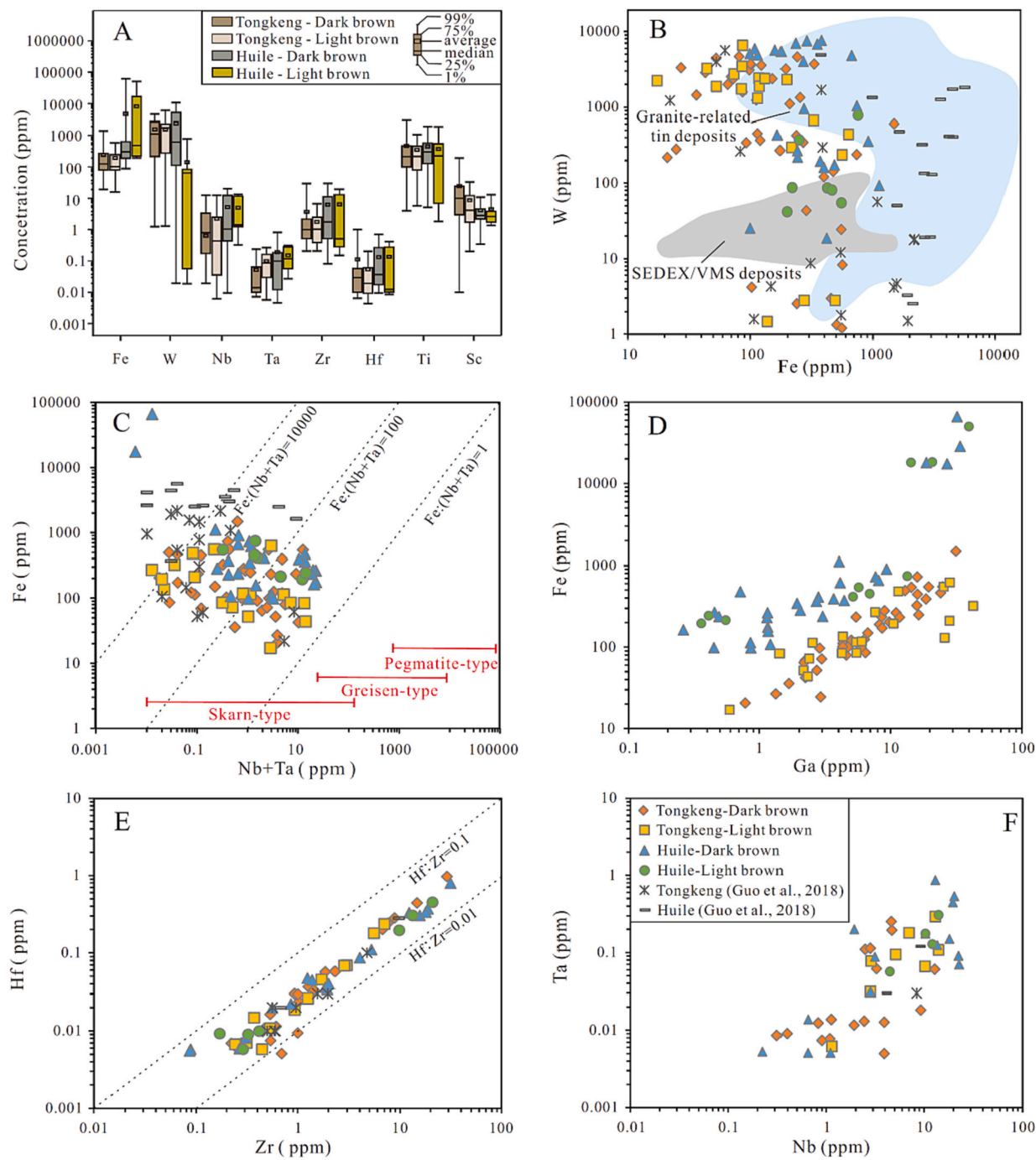


Fig. 6. Box-and -whisker diagram (A) and binary plots (B-F) of selected elements in cassiterites from the Tongkeng and Huile deposits in the Dachang district. Previously reported cassiterite data of the Tongkeng and Huile deposits from Guo et al. (2018a) are also plotted for comparison. Constructed areas of granite-related and SEDEX/VMS tin deposits in (B) are modified after Guo et al. (2018a). Typical ranges of Nb + Ta concentrations of skarn-, greisen- and pegmatite-type cassiterite in (C) are sourced from Pavlova et al. (2015), Fuchsloch et al. (2019), Hulsbosch and Muchez (2020), Chen et al. (2019), Cheng et al. (2019), and Chen et al. (2022).

orebodies away from its parental magma requires high flux fluid conduits that can efficiently transfer massive amount of ore-forming fluids until they reach position and condition favorable for ore mineral precipitation. The steeply dipping dike-hosting faults and their substructures are probably indispensable for the formation of the massive cassiterite-sulfide mineralization by providing fluid conduits down to the granite and enhancing the permeability of the host sedimentary strata. Combined with the geochronological constraint, we therefore propose that the dike-hosting faults are very likely served as the conduits for ore fluids and its surrounding host rocks are potential target for ore exploration in the district.

The Huile deposit in the east part of the Dachang district is characterized by cassiterite-sulfide quartz veins that resembles the upper vein-type mineralization in the Tongkeng deposit (Xie, 2017). Although no porphyritic dike or granite is yet discovered in the deposit, the identical mineral assemblage and cassiterite ages indicate that the Huile and Tongkeng deposit were formed broadly in response to the same district-scale granitic magmatism which may have generated several individual hydrothermal ore systems under favorable structure and host rock conditions. This opens new exploration potential for proximal ores in the deep part of the Huile deposit.

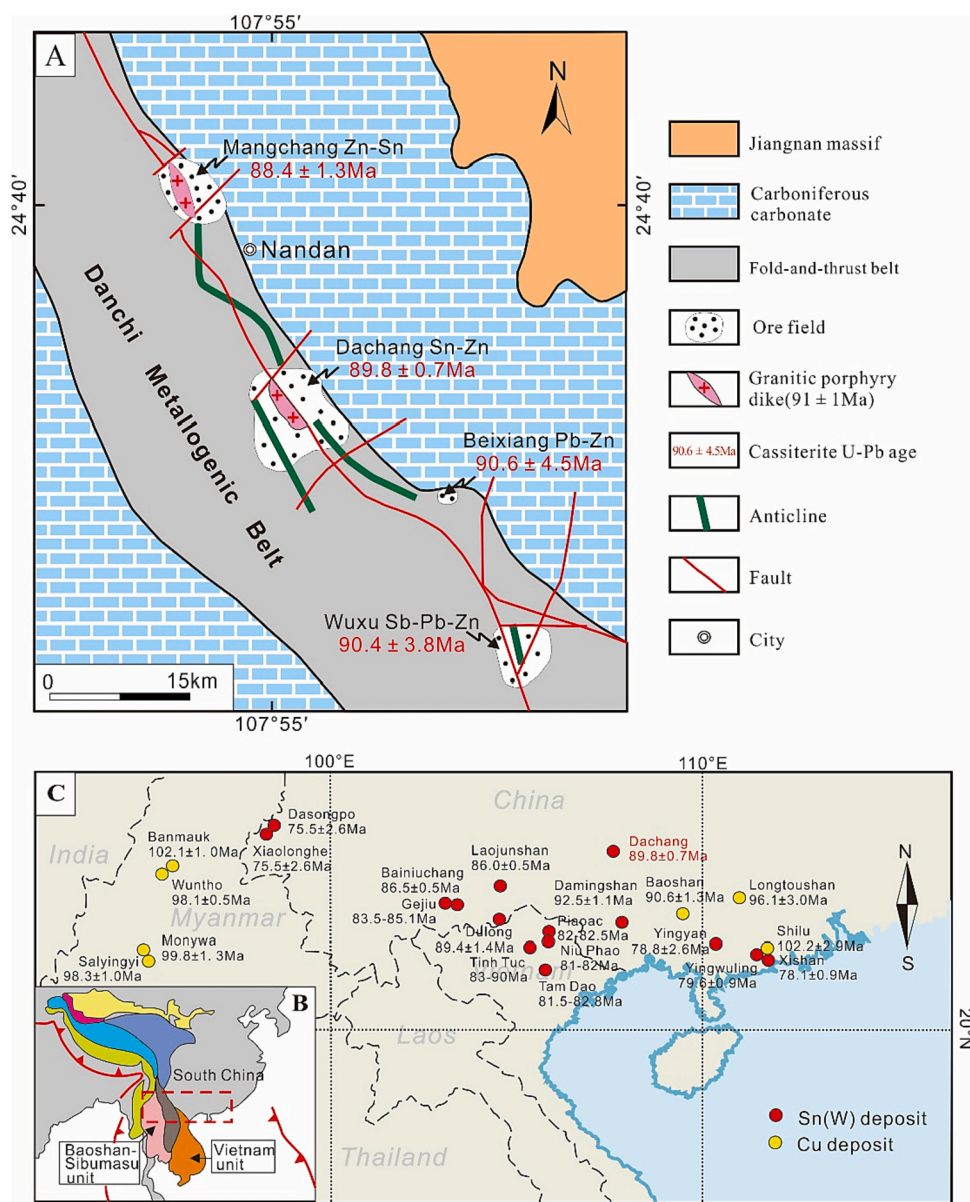


Fig. 7. Schematic map showing the distributions of tin deposits with their cassiterite U-Pb ages in the Danchi metallogenetic belt and the granitic porphyry dikes (A), and Cretaceous Cu and Sn deposits in southwest China, northern Vietnam, and Myanmar (B and C; modified from Huang et al., 2019). The cassiterite age of the Dachang is from this study, Mangchang from Liao et al., unpublished data, Beixiang from Wu et al. (2022), and Wuxu from Xiao et al. (2022). Other data are compiled by Huang et al. (2019).

7. Conclusions

This study presents new in-situ trace element compositions and U-Pb ages of cassiterites from the Tongkeng and Huile tin-polymetallic deposits in the Dachang district. The trace element signature of cassiterites indicate a granitic magmatic hydrothermal environment that are similar to skarn-related tin deposits. Cassiterite U-Pb dating obtained from near 400 spot analyses demonstrates that they were formed within a narrow time period from 91 to 89 Ma, which is identical to the mineralization ages of the Danchi Sn-polymetallic belt in the region (Fig. 7A). The obtained mineralization ages of the Tongkeng and Huile deposits are substantially younger than the dominated equigranular phase of the Longxianggai pluton, but they agree well with the emplacement ages of the porphyritic granite represented either by the latest phase of the Longxianggai granite or the granite porphyry dikes (ca. 91 Ma). These ages together with geological context suggest that the tin-polymetallic deposits in the Dachang district were most likely produced by a magmatic hydrothermal system intimately related to later, higher evolved granitic phases which also generated skarn type Zn-Cu mineralization in the district. We propose that the dike-hosting faults

were most likely served as the conduits for ore fluids and its surrounding host rocks are potential targets for ore exploration in the Dachang district.

Declaration of competing interest

The authors declare the following financial interests/personal relationships which may be considered as potential competing interests: Wenchao Su reports financial support was provided by National Natural Science Foundation of China. Junyi Pan reports financial support was provided by Nanjing University.

Data availability

Data will be made available on request.

Acknowledgments

We are grateful to Guangxi Tongkeng Mining Company for access to samples. We would like to thank Dr. Yuexing Feng and Chunhui Zhu for

help with LA-ICP-MS analysis. This work was supported by the National Natural Science Foundation of China (92062220, 41672080, 42263009) and a Fundamental Research Funds for the Central Universities (020614380117).

References

- Bendezú, R., Fontboté, L., Cosca, M., 2003. Relative age of Cordilleran base metal lode and replacement deposits, and high sulfidation Au-(Ag) epithermal mineralization in the Colquijirca mining district, central Peru. *Mineral. Deposita* 38, 683–694.
- Cai, H.Y., Zhang, G.L., 1983. On submarine volcanism hot spring (exhalative) mineralization of the Dachang tin polymetallic deposit in Guangxi. *J. Coll. Miner. Geol.* 4, 13–21 (in Chinese).
- Cai, M.H., Liang, T., Wu, D.C., Huang, H.M., 2004. Structure characteristics and mineralization controls of the Nandan-Hechi metallogenic belt in Guangxi Province. *Geol. Prospect.* 40, 5–10 (in Chinese with English abstract).
- Cai, M.H., Liang, T., Wu, D.C., 2005. Geological characteristics and ore-forming time of the Kangma deposit in the Dachang tin-polymetallic ore field, Guangxi. *Acta Geol. Sin.* 79, 262–268 (in Chinese with English abstract).
- Cai, M.H., He, L.Q., Liu, G.Q., Wu, D.C., Huang, H.M., 2006a. SHRIMP zircon U-Pb dating of the intrusive rocks in the Dachang tin-polymetallic ore field, Guangxi and their geological significance. *Geol. Rev.* 52, 409–414 (in Chinese with English abstract).
- Cai, M.H., Liang, T., Wei, K.L., Huang, H.M., Liu, G.Q., 2006b. Rb-Sr dating of the No. 92 orebody of the Tongkeng-Changpo deposit in the Dachang tin polymetallic ore field, Guangxi, and its significance. *Geol. Miner. Resour. South China* 2, 31–36 (in Chinese with English abstract).
- Cai, M.H., Mao, J.W., Liang, T., Pirajno, F., Huang, H.L., 2007. The origin of the Tongkeng-Changpo tin deposit, Dachang metal district, Guangxi, China: clues from fluid inclusions and he isotope systematics. *Mineral. Deposita* 42, 613–626.
- Cai, M.H., Peng, Z.N., Hu, Z.S., Li, Y., 2020. Zn, He-Ar and Sr-Nd isotopic compositions of the Tongkeng tin-polymetallic ore deposit in South China: implication for ore genesis. *Ore Geol. Rev.* 124, 103605.
- Cao, H.W., Zou, H., Zhang, Y.H., Zhang, S.T., Zheng, L., Zhang, L.K., Tang, L., Pei, Q.M., 2016. Late cretaceous magmatism and related metallogenesis in the Tengchong area: evidence from geochronological, isotopic and geochemical data from the Xiaolonghe Sn deposit, western Yunnan, China. *Ore Geol. Rev.* 78, 196–212.
- Cathles, L.M., Erendi, A.H.J., Barrie, T., 1997. How long can a hydrothermal system be sustained by a single intrusive event? *Econ. Geol.* 92, 766–771.
- Chen, Y.C., Huang, M.Z., Xu, J., Ai, Y.D., Li, X.M., Tang, S.H., Meng, L.K., 1985. Geological features and metallogenic series of the Dachang cassiterite-sulfide-polymetallic belt. *Acta Geol. Sin.* 3, 228–240 (in Chinese with English abstract).
- Chen, Y.C., Huang, M.Z., Xu, J., Hu, Y.Z., Tang, S.H., Li, Y.Q., Meng, L.K., 1993. *Geology of Dachang Tin Deposit*. Geological Publishing House, Beijing (in Chinese).
- Chen, L.L., Ni, P., Dai, B.Z., Li, W.S., Chi, Z., Pan, J.Y., 2019. The genetic association between quartz vein- and greisen-type mineralization at the Maoping W-Sn deposit, southern Jiangxi, China: insights from zircon and cassiterite U-Pb ages and cassiterite trace element composition. *Minerals* 9, 411.
- Chen, S.C., Yu, J.J., Bi, M.F., Li, H.M., Lehmann, B., 2022. Cassiterite U-Pb, mica 40Ar–39Ar dating and cassiterite trace-element composition of the Furong tin deposit in the Nanling Range, South China. *Ore Geol. Rev.* 143, 104775.
- Cheng, Y.B., Mao, J.W., Liu, P., 2016. Geodynamic setting of Late Cretaceous Sn-W mineralization in southeastern Yunnan and northeastern Vietnam. *Solid Earth Sci.* 1, 79–88.
- Cheng, Y.B., Spandler, C., Kemp, A., Mao, J.W., Rusk, B., Hu, Y., Blake, K., 2019. Controls on cassiterite (SnO₂) crystallization: evidence from cathodoluminescence, trace-element chemistry, and geochronology at the Gejiu tin district. *Am. Mineral.* 104, 118–129.
- Chiariadis, M., Schaltegger, U., Spikings, R., Wotzlaw, J.F., Ovtcharova, M., 2012. How accurately can we date the duration of magmatic-hydrothermal events in porphyry system? – an invited paper. *Econ. Geol.* 108, 565–584.
- Denholm, J.L., Stepanov, A.S., Meffre, S., Bottrill, R.S., Thompson, J.M., 2021. The geochronology of Tasmanian tin deposits using LA-ICP-MS U-Pb cassiterite dating. *Econ. Geol.* 116, 1387–1407.
- Fan, D.L., Zhang, T., Ye, J., Pašava, J., Kribek, B., Dobes, P., Varrin, I., Zak, K., 2004. Geochemistry and origin of tin-polymetallic sulfide deposits hosted by the Devonian black shale series near Dachang, Guangxi, China. *Ore Geol. Rev.* 24, 103–120.
- Fu, M., Changkakoti, A., Krouse, H.R., Gray, J., Kwak, T.A.P., 1991. An oxygen, hydrogen, sulfur, and carbon isotopic study of carbonate-replacement (skarn) tin deposits of the Dachang tin field, China. *Econ. Geol.* 86, 1683–1703.
- Fu, M., Kwak, T.A.P., Mernagh, T.P., 1993. Fluid inclusion studies of zoning in the Dachang tin-polymetallic ore field, People's Republic of China. *Econ. Geol.* 88, 283–300.
- Fuchsloch, W.C., Nex, P.A.M., Kinnaird, J.A., 2019. The geochemical evolution of Nb-Ta-Sn oxides from pegmatites of the Cape Cross-Uis pegmatite belt, Namibia. *Mineral. Mag.* 83, 161–179.
- Gardiner, N.J., Robb, L.J., Morley, C.K., Searle, M.P., Cawood, P.A., Whitehouse, M.J., Kirkland, C.L., Roberts, N.M.W., Myint, T.A., 2016. The tectonic metallogenic framework of Myanmar: a Tethyan mineral system. *Ore Geol. Rev.* 79, 26–45.
- Gemmrich, L., Torró, L., Melgarejo, J.C., Laurent, O., Vallance, J., Chelle-Michou, C., Sempre, T.P.A., 2021. Trace element composition and U-Pb ages of cassiterite from the Bolivian tin belt. *Mineral. Deposita* 56, 1491–1520.
- Guo, J., Zhang, R.Q., Sun, W.D., Ling, M.X., Hu, Y.B., Wu, K., Luo, M., Zhang, L.C., 2018a. Genesis of tin-dominant polymetallic deposits in the Dachang district, South China: insights from Cassiterite U-Pb ages and trace element compositions. *Ore Geol. Rev.* 95, 863–879.
- Guo, J., Zhang, R.Q., Li, C.Y., Sun, W.D., Hu, Y.B., Kang, D.M., Wu, J.D., 2018b. Genesis of the Gaosong Sn-Cu deposits, Gejiu district, SW China: constraints from *in situ* LA-ICP-MS cassiterite U-Pb dating and trace element fingerprinting. *Ore Geol. Rev.* 92, 627–642.
- Han, F., Hutchinson, R.W., 1989a. Evidence for exhalative origin for rocks and ores of the Dachang tin polymetallic field: the ore-bearing formation and hydrothermal exhalative sedimentary rocks. *Mineral Deposits* 8, 25–40 (in Chinese with English abstract).
- Han, F., Hutchinson, R.W., 1989b. Evidence for hydrothermal exhalative sedimentary origin of the Dachang tin-polymetallic deposits- geochemistry of rare earth elements and trace elements of the host rocks. *Mineral Deposits* 8, 33–42 (in Chinese with English abstract).
- Han, F., Zhao, R.S., Shen, J.Z., Hutchinson, R.W., Jiang, S.Y., 1997. *Geology and Origin of Ores in the Dachang Polymetallic Tin Ore Field*. Geological Publishing House, Beijing (in Chinese).
- Hennigh, Q.T., Hutchinson, R.W., 1999. Cassiterite at Kidd Creek: an example of volcanogenic massive sulfide-hosted tin mineralization. *Soc. Econ. Geol.* 10, 431–440.
- Hoskin, P.W.O., Schaltegger, U., 2003. The composition of zircon and igneous and metamorphic petrogenesis. *Rev. Mineral. Geochem.* 53, 27–62.
- Huang, W.H., Fan, S.K., Chen, C.W., Bi, Z.M., 2012. Application of metallogenic regularity to study of skarn zinc-copper deposits in Dachang orefield: a case study of Heishuiogu-Dashujiao and Yangjiaojiao skarn zinc-copper deposits. *Mineral Deposits* 31, 535–544 (in Chinese with English abstract).
- Huang, W.T., Liang, H.Y., Zhang, J., Wu, J., Chen, X.L., Ren, L., 2019. Genesis of the Dachang Sn-polymetallic and Baoshan Cu ore deposits, and formation of a cretaceous Sn-Cu ore belt from southwest China to western Myanmar. *Ore Geol. Rev.* 112, 103030.
- Hulsbosch, N., Muchez, P., 2020. Tracing fluid saturation during pegmatite differentiation by studying the fluid inclusion evolution and multiphase cassiterite mineralisation of the Gatumba pegmatite dyke system (NW Rwanda). *Lithos* 354–355, 105285.
- Jiang, S.Y., Han, F., Shen, J.Z., Palmer, M.R., 1999. Chemical and Rb-Sr, Sm-Nd isotopic systematics of tourmaline from the Dachang Sn-polymetallic ore deposit, Guangxi province, P.R.China. *Chem. Geol.* 157, 49–67.
- Li, H.Q., Wang, D.H., Mei, Y.P., Liang, T., Cheng, Z.Y., Guo, C.L., Ying, L.J., 2008. Lithogenesis and mineralization chronology study on the Lamo zinc-copper polymetallic ore deposit in Dachang orefield, Guangxi. *Acta Geol. Sin.* 82, 912–920 (in Chinese with English abstract).
- Li, Z., Qiu, J.S., Yang, X.M., 2014. A review of the geochronology and geochemistry of Late Yanshanian (Cretaceous) pluton along the Fujian coastal area of southeastern China: implications for magma evolution related to slab break-off and rollback in the Cretaceous. *Earth Sci. Rev.* 128, 232–248.
- Li, C.Y., Zhang, R.Q., Ding, X., Ling, M.X., Fan, W.M., Sun, W.D., 2016. Dating cassiterite using laser ablation ICP-MS. *Ore Geol. Rev.* 72, 313–322.
- Li, Y., Allen, M.B., Li, X.H., 2022. Millennial pulses of ore formation and an extra-high Tibetan Plateau. *Geology* 50, 665–669.
- Liang, T., Chen, Y.C., Wang, D.H., Cai, M.H., 2008. *The Geological and Geochemical Characteristics of Dachang Tin-polymetallic Deposit*, Guangxi. Geological Publishing House, Beijing (in Chinese).
- Liang, T., Wang, D.H., Hou, K.J., Li, H.Q., Huang, H.M., Cai, M.H., Wang, D.M., 2011. LA-MC-ICP-MS zircon U-Pb dating of Longxianggai pluton in Dachang of Guangxi and its geological significance. *Acta Petrol. Sin.* 27, 1624–1636 (in Chinese with English abstract).
- Ludwig, K.R., 2003. In: *User's Manual for Isoplot 3.00: A Geochemical Toolkit for Microsoft Excel*. Berkeley Geochronology Center, p. 4.
- Ma, N., Deng, J., Wang, Q.F., Wang, C.M., Zhang, J., Li, G.J., 2013. Geochronology of the Dasongpo tin deposit, Yunnan Province: evidence from zircon LA-ICP-MS U-Pb ages and cassiterite LA-MC-ICP-MS U-Pb ages. *Acta Petrol. Sin.* 29, 1223–1235 (in Chinese with English abstract).
- Mao, J.W., Cheng, Y.B., Guo, C.L., Yang, Z.X., Peng, J.R., 2008. Gejiu tin polymetallic ore field: deposit model discussion for several points concerned. *Acta Geol. Sin.* 82, 1455–1467 (in Chinese with English abstract).
- Mao, J.W., Pirajno, F., Cook, N., 2011. Mesozoic metallogenesis in East China and corresponding geodynamic setting – an introduction to the special issue. *Ore Geol. Rev.* 43, 1–7.
- Möller, P., Dulski, P., Szacki, W., Malow, G., Riedel, E., 1988. Substitution of tin in cassiterite by tantalum, niobium, tungsten, iron, and manganese. *Geochim. Cosmochim. Acta* 52, 1497–1503.
- Moore, F., Howie, R.A., 1979. *Geochemistry of some Cornubia cassiterites*. *Mineral. Deposita* 14, 103–107.
- Muntean, J.L., Einaudi, M.T., 2001. Porphyry-epithermal transition: Maricunga belt, northern Chile. *Econ. Geol.* 96, 743–772.
- Murciego, A., Sanchez, A.G., Dusausoy, Y., Pozas, J.M., Ruck, R., 1997. *Geochemistry and EPR of cassiterites from the Iberian Hercynian Massif*. *Mineral. Mag.* 61, 357–365.
- Pan, J.Y., Ni, P., Chi, Z., Wang, W.B., Zeng, W.C., Xue, K., 2019. Alunite 40Ar/39Ar and zircon U-Pb constraints on the magmatic-hydrothermal history of the Zijinshan high-sulfidation epithermal Cu-Au deposit and the adjacent Luoboling porphyry Cu-Mo deposit, South China: implications for their genetic association. *Econ. Geol.* 114, 667–695.
- Pašava, J., Kribek, B., Dobes, P., Vavřín, I., Žák, K., Fan, D.L., Zhang, T., Boiron, M.C., 2003. Tin-polymetallic sulfide deposits in the eastern part of the Dachang tin field

- (South China) and the role of black shales in their origin. *Mineral. Deposita* 38, 39–66.
- Paton, C., Hellstrom, J., Paul, B., Woodhead, J., Hergt, J., 2011. Iolite: freeware for the visualization and processing of mass spectrometric data. *J. Anal. At. Spectrom.* 26, 2508–2518.
- Pavlova, G.G., Palessky, S.V., Borisenko, A.S., Vladimirov, A.G., Seifert, T., Phan, L.A., 2015. Indium in cassiterite and ores of tin deposits. *Ore Geol. Rev.* 66, 99–113.
- Pettke, T., Diamond, L.W., 1995. Rb-Sr isotopic analysis of fluid inclusions in quartz: evaluation of bulk extraction and procedures and geochronometer systematics using synthetic fluid inclusions. *Geochim. Cosmochim. Acta* 59, 4009–4027.
- Pieczka, A., Gołębowska, B., Parafiniuk, J., 2007. Geochemistry and origin of the cassiterite from Rędziny, lower Silesia, Poland. *Mineral. Pol.* 38, 219–228.
- Plimer, I.R., Lu, J., Kleeman, J.D., 1991. Trace and rare earth elements in cassiterite—sources of components for the tin deposits of the Mole Granite, Australia. *Mineral. Deposita* 26, 267–274.
- Quadt, A., Erni, M., Martinek, K., Moll, M., Peytcheva, I., Heinrich, C.A., 2011. Zircon crystallization and the lifetimes of ore-forming magmatic-hydrothermal systems. *Geology* 39, 731–734.
- Roger, F., Maluski, H., Lepvrier, C., Van, T.V., Paquette, J.L., 2012. LA-ICPMS zircon U/Pb dating of Permo-Triassic and Cretaceous magmatism in the Northern Vietnam—geodynamic implication. *J. Asian Earth Sci.* 48, 72–82.
- Rubin, J.N., Henry, C.D., Price, J.G., 1993. The mobility of zirconium and other immobile elements during hydrothermal alteration. *Chem. Geol.* 110, 29–47.
- Schneider, H.J., Dulski, P., Luck, J., Moeller, P., Villapando, A., 1978. Correlation of trace element distribution in cassiterites and geotectonic position of their deposits in Bolivia. *Mineral. Deposita* 13, 119–122.
- Shannon, R.D., 1976. Revised effective ionic radii and systematic studies of interatomic distances in halides and chalcogenides. *Acta Crystallogr. A* 751–767.
- Stevenson, B.G., Taylor, R.G., 1973. Trace element content of some cassiterites from Eastern Australia. *Proc. R. Soc. Queensland* 84, 43–54.
- Sun, W.D., 2016. Initiation and evolution of the South China Sea: an overview. *Acta Geochim.* 35, 215–225.
- Sun, W.D., Ding, X., Hu, Y.H., Li, X.H., 2007. The golden transformation of the Cretaceous plate subduction in the west Pacific. *Earth Planet. Sci. Lett.* 262, 533–542.
- Taylor, R.G., 1979. *Geology of Tin Deposits*. Elsevier Science.
- Tindle, A.G., Breaks, F.W., 1998. Oxide minerals of the separation rapids rare-element granitite pegmatite group, northwestern Ontario. *Can. Mineral.* 36, 609–635.
- Wang, D.H., Chen, Y.C., Chen, W., Sang, H.Q., Li, H.Q., Lu, Y.F., Chen, K.L., Lin, Z.M., 2004. Dating the Dachang giant tin-polymetallic deposit in Nandan, Guangxi. *Acta Geol. Sin.* 78, 132–138 (in Chinese with English abstract).
- Wang, X.Y., Huang, H.W., Chen, N.S., Huang, X.Q., Wu, X.K., Hao, S., Li, H.M., 2015. In-situ LA-MC-ICPMS U-Pb geochronology of cassiterite from Changpo-Tongkeng tin-polymetallic deposits, Dachang ore field, Guangxi. *Geol. Rev.* 61, 892–900 (in Chinese with English abstract).
- Wu, J., Yuan, H.W., Gan, N.J., Wei, S.C., Liao, J., Zhang, J., Liang, H.Y., 2020. Source characteristics of magmatic rocks and zircon U-Pb age in the Mangchang ore field, Danchi metallogenic belt, Guangxi. *Acta Petrol. Sin.* 36, 1586–1596 (in Chinese with English abstract).
- Wu, J., Li, Z., Zhu, M.J., Huang, W.T., Liao, J., Zahng, J., Liang, H.Y., 2022. Genesis of the Beixiang Sb-Pb-Zn-Sn deposit and polymetallic enrichment of the Danchi Sn-polymetallic ore belt in Guangxi, SW China. *Minerals* 12, 1349.
- Xiao, C.H., Chen, Z.L., Liu, X.C., Wei, X.S., Wu, Y., Tang, Y.W., Wang, X.Y., 2022. Structural analysis, mineralogy, and cassiterite U-Pb ages of the Wuxu Sb-Zn-polymetallic district, Danchi fold-and thrust belt, South China. *Ore Geol. Rev.* 150, 105150.
- Xie, P., 2017. The Geochemistry of Ore-forming Fluid of Huile and Kangma Tin-polymetallic Deposits in the Dachang Ore Field, Guangxi, China. Unpublished Master dissertation. Institute of Geochemistry, Chinese Academy of Sciences, Guiyang, China (in Chinese with English abstract).
- Xu, M., Cai, M.H., Peng, Z.A., Zhang, S.Q., Chen, Y., Wang, X.B., 2011. Characteristics of structures and controls on mineralization of Tongkeng tin-polymetallic deposit in Guangxi. *Geotecton. Metallog.* 35, 587–595 (in Chinese with English abstract).
- Yuan, S.D., Peng, J.T., Hu, R.Z., Li, H.M., Shen, N.P., Zhang, D.L., 2008. A precise U-Pb age on cassiterite from the Xianghualing tin-polymetallic deposit (Hunan, South China). *Minerlium Deposita* 43, 375–382.
- Yuan, S.D., Peng, J.T., Hao, S., Li, H.M., Geng, J.Z., Zhang, D.L., 2011. In situ LA-MC-ICP-MS and ID-TIMS U-Pb geochronology of cassiterite in the giant Furong tin deposit, Hunan Province, South China: new constraints on the timing of tin-polymetallic mineralization. *Ore Geol. Rev.* 43, 235–242.
- Zhang, R.Q., Lu, J.J., Wang, R.C., Yang, P., Zhu, J.C., Yao, Y., Gao, J.F., Li, C., Lei, Z.H., Zhang, W.L., 2015. Constraints of in situ zircon and cassiterite U-Pb, molybdenite Re-Os and muscovite 40Ar-39Ar ages on multiple generations of granitic magmatism and related W-Sn mineralization in the Wangxianling area, Nanling Range, South China. *Ore Geol. Rev.* 65, 1021–1042.
- Zhang, L.P., Hu, Y.B., Liang, J.L., Ireland, T., Zhang, R.Q., Sun, S.J., Sun, W.D., 2017a. Adakitic rocks associated with the Shilu copper-molybdenum deposit in the Yangchun Basin, South China, and their tectonic implications. *Acta Geochim.* 36, 132–150.
- Zhang, L.P., Zhang, R.Q., Hu, Y.B., Liang, J.L., Ouyang, Z., He, J.J., Chen, Y.X., Guo, J., Sun, W.D., 2017b. The formation of the late Cretaceous Xishan Sn-W deposit, South China: geochronological and geochemical perspectives. *Lithos* 290–291, 253–268.
- Zhang, R.Q., Lu, J.J., Lehmann, B., Li, C.Y., Li, G.L., Zhang, L.P., Guo, J., Sun, W.D., 2017a. Combined zircon and cassiterite U-Pb dating of the Piaotang granite-related tungsten-tin deposit, southern Jiangxi tungsten district, China. *Ore Geol. Rev.* 82, 268–284.
- Zhang, R.Q., Lehmann, B., Seltmann, R., Sun, W.D., Li, C.Y., 2017b. Cassiterite U-Pb geochronology constrains magmatic-hydrothermal evolution in complex evolved granite systems: the classic Erzgebirge tin province (Saxony and Bohemia). *Geology* 45, 1095–1098.
- Zhang, L.P., Zhang, R.Q., Wu, K., Chen, Y.X., Li, C.Y., Hu, Y.B., He, J.J., Liang, J.L., Sun, W.D., 2018. Late cretaceous granitite magmatism and mineralization in the Yingwuling W-Sn deposit, South China: constraints from zircon and cassiterite U-Pb geochronology and whole-rock geochemistry. *Ore Geol. Rev.* 96, 115–129.
- Zhang, Z.Q., Bagas, L., Mao, J.W., Chen, M.H., Fu, B., 2018. Mineralisation associated with the fractionated Cretaceous Baoshan Monzogranite: tectonic implications for South China. *Ore Geol. Rev.* 102, 791–810.
- Zhang, L.P., Zhang, R.Q., Chen, Y.X., Sun, S.J., Liang, J.L., Sun, W.D., 2019. Geochronology and geochemistry of the late Cretaceous Xinpeng granitic intrusion, South China: implication for Sn-W mineralization. *Ore Geol. Rev.* 113, 103705.
- Zhao, H., 2018. Hydrothermal Fluids and Ore-formation of Tongkeng and Gaofeng Tin-polymetallic Deposits in the Dachang Ore Field, Guangxi, China. Unpublished Ph.D. dissertation. Institute of Geochemistry, Chinese Academy of Sciences, Guiyang, China (in Chinese with English abstract).
- Zhao, K.D., Jiang, S.Y., Xiao, H.Q., Ni, P., 2002. Origin of ore-forming fluids of the Dachang Sn-polymetallic ore deposit: evidence from helium isotopes. *Chin. Sci. Bull.* 47, 1041–1045.
- Zhao, K.D., Jiang, S.Y., Ni, P., Ling, H.F., Jiang, Y.H., 2007. Sulfur, lead and helium isotopic compositions of sulfide minerals from the Dachang Sn-polymetallic ore district in South China: implication for ore genesis. *Mineral. Petrol.* 89, 251–273.
- Zhao, H., Su, W.C., Xie, P., Shen, N.P., Cai, J.L., Luo, M., Bao, Z., 2018. Re-Os dating of molybdenite and in-situ Pb isotopes of sulfides from the Lamo Zn-Cu deposit in the Dachang Tin-polymetallic ore field, Guangxi, China. *Acta Geochim.* 37, 384–394.